J. Fluid Mech. (2021), *vol*. 909, A15. © The Author(s), 2020.
Published by Cambridge University Press
doi:10.1017/jfm.2020.923

Bypass transition in flow over a vibrating flat plate

Wenlin Huang[1], **Dandan Xiao**[2], **Jie Ren**[2], **Zhiheng Wang**[1,†], **Guang Xi**[1] **and Xuerui Mao**[2]

[1]School of Energy and Power Engineering, Xi'an Jiaotong University, Xi'an, Shaanxi, 710049, PR China
[2]Faculty of Engineering, University of Nottingham, Nottingham NG7 2RD, UK

(Received 5 June 2020; revised 15 September 2020; accepted 19 October 2020)

The development of free-stream disturbances in flow over a vertically vibrating flat plate with a slender leading edge is investigated. The evolution of the optimal inflow perturbation that results in the maximum amplification is computed to investigate the effect of the plate vibration on the development of free-stream disturbance, secondary instability of streaks and subsequently the bypass transition to turbulence. It is observed that the plate vibration leads to periodic change of the angle of attack, shifting the free-stream disturbance to the upper or lower side of the plate. Therefore, the development of steady inflow perturbations, which receive the largest amplification, is interrupted by the vibration, and the perturbation amplification via the lift-up mechanism is weakened. The vibration brings a second peak of perturbation growth at the vibration frequency, leading to high-frequency free-stream perturbations penetrating into the base boundary layer, which is not observed in flow over a stationary plate owing to the sheltering mechanism. This resonance of the flow perturbation and the vibrating plate is explained by the staggering effect of the leading edge. Further, the direct numerical simulations with the optimal inflow perturbation imposed on the inflow boundary show that the vertical vibration of the plate leads to streamwise periodic vorticity near the edge of the boundary layer. This inhomogeneity of the streamwise vorticity brings about streamwisely localized distortion of the low-speed streaks and, thus, an intermittent secondary instability. Therefore, before the streaks break down to turbulence, they undergo several rounds of secondary instabilities, resulting in an elongated bypass transition process.

Key words: transition to turbulence, flow–structure interactions, boundary-layer stability

1. Introduction

Bypass transition in boundary-layer flow receives its name mainly from the bypass of Tollmien–Schlichting (TS) waves (Morkovin 1969). This scenario of transition occurs when the turbulence intensity level of the free-stream disturbance is above 0.5 %. Research on bypass transition is far-reaching in boundary-layer flow around fixed streamlined bodies such as flat plates, airfoils and turbine blades, focusing on the development of large and streamwisely elongated coherent structures, namely, the velocity streaks (Kendall 1985; Westin *et al.* 1994; Alfredsson & Matsubara 1996). The present work addresses

† Email address for correspondence: wangzhiheng@mail.xjtu.edu.cn

bypass transition in flow around a vibrating flat plate, which is of significant importance as vibrations and resonances in fluid–structure interactions are ubiquitous in nature and engineering applications (for example, the boundary-layer flow around a vibrating aircraft wing). In the following, previous studies on bypass transition and flows around vibrating bodies are reviewed briefly in §§ 1.1 and 1.2, respectively, before introducing the motivation of the present work in § 1.3.

1.1. *Bypass transition in boundary-layer flow*

The early stage of bypass transition in a boundary-layer flow involves the interaction of incoming disturbances with the laminar shear profile via the lift-up mechanism, giving rise to amplified streamwise-elongated velocity streaks (Landahl 1975, 1980), as being addressed in parallel flows (Butler & Farrell 1992; Reddy & Henningson 1993) as well as in non-parallel flat-plate boundary-layer flow (Andersson, Berggren & Henningson 1999; Luchini 2000; Monokrousos *et al.* 2010). In the lift-up, the streamwise vorticity perturbations displace low-momentum fluid upwards and sweep the high-momentum fluid toward the wall, thus creating the low- and high-speed streaks. This evolution of perturbations from streamwise vorticity to streamwise velocity is clearly non-modal, and therefore transient growth analyses have been applied extensively to compute the optimal inflow or initial disturbances that lead to the strongest generation of streaks. The spanwise wavenumber of the optimal perturbation calculated from the transient growth analyses is consistent with experimental observations (Matsubara & Alfredsson 2001; Mandal, Venkatakrishnan & Dey 2010; Nolan & Walsh 2012) and direct numerical simulations (DNS) (Jacobs & Durbin 2001; Nagarajan, Lele & Ferziger 2007). Applying the transient growth analyses method, Brandt *et al.* (2011) found that the optimal perturbation growth via the lift-up mechanism is robust and insensitive to the modification of the base shear. It is also found that the lift-up effect maximizes when the streamwise vorticity is steady and degrades at increasing frequency of this vorticity (Monokrousos *et al.* 2010; Wang, Mao & Zaki 2019). The appearance of the steady or low-frequency streaks is further explained by the shear sheltering mechanism in the boundary layer (Hunt & Durbin 1999; Zaki & Saha 2009).

After the formation and amplification of streaks via the linear lift-up mechanism, the next stage of bypass transition is the nonlinear deformation of streaks and their secondary instabilities. The interaction between the streaks and the streamwise vorticity lifts the low- (or high-)speed streaks away from (or towards) the wall via a nonlinear lift-up mechanism, resulting in a mean shear profile with an inflection point, which is prone to shear flow instabilities (Mao *et al.* 2017). The lifted low-speed streaks are also exposed to the high-frequency free-stream disturbances near the top of boundary layer, activating secondary instabilities of streaks (Jacobs & Durbin 2001; Brandt, Schlatter & Henningson 2004; Zaki & Durbin 2005). Swearingen & Blackwelder (1987) identified two types of secondary instabilities of streaks in Görtler flow: sinuous mode and varicose mode, referring to spanwisely symmetric and asymmetric forms of the unstable modes, respectively. These two types of instability are confirmed in the experiments using dye visualization (Matsubara & Alfredsson 2001; Asai, Minagawa & Nishioka 2002; Mans *et al.* 2005) and a simultaneous dual plane particle image velocimetry measurements technique (Balamurugan & Mandal 2017). Sinuous instability occurs at the top of the boundary layer and is related to the velocity inflection point in the spanwise direction. The varicose counterpart occurs at the overlapped region of high- and low-speed streaks and is related to the inflection point in the wall-normal direction (Zaki & Durbin 2006). In general, the sinuous mode is more common and dangerous because it occurs at lower

streak amplitude (26 % of the free-stream velocity), compared with 37 % of the free-stream velocity for the varicose mode (Andersson *et al.* 2001). Considering the height of the critical layer from the wall, Vaughan & Zaki (2011) classified the instabilities of streaks into another two types: inner mode and outer mode. The outer mode is related to the secondary instability of the lifted low-speed streaks, whereas the inner mode resides near the wall resembling the classical TS waves. They also reported a much smaller critical amplitude of streak (15.2 % of the free-stream velocity) to activate the outer mode (sinuous type) secondary instability because the spanwise shear is stronger for the same streak amplitude in their case. Further development of the secondary instabilities will induce the breakdown of streaks and generation of turbulent spots, leading to the bypass transition to turbulence.

1.2. *Vibration of solid body and its induced flow instability*

The studies of fluid flows around a vibrating solid body and the associated fluid and structure interactions are rich. The vibration can be in the streamwise, wall-normal or spanwise directions. Early studies mainly focused on flows around bluff bodies, e.g. circular cylinders vibrating in the cross-flow direction, addressing the interaction of the body motion with the downstream vortex shedding (Riley 1965, 1967; Olinger & Sreenivasan 1988). In boundary-layer flow, Spalart (1989) found that the continuously changing mean flow direction suppressed the streak-like elongated structure. Later, Jung, Mangivacchi & Akhavan (1992) studied the turbulent channel flow with the wall vibrating in spanwise direction, and reported a drag reduction up to 40 %. Inspired by Jung *et al.* (1992), the spanwise wall vibration is further investigated extensively for turbulence suppression and drag reduction (Laadhari, Skandaji & Morel 1994; Baron & Quadrio 1996; Karniadakis & Choi 2003). Choi (2002) demonstrated that the wall vibration weakens the transportation of high-speed fluids toward the wall, hampering the stretching of the quasi-streamwise vortices in the near-wall region, and thereby reducing the streamwise vorticity. Consequently, the near-wall burst event is weakened and turbulent skin-friction is reduced. The effect of the spanwise wall vibration on turbulent streaks was studied by Touber & Leschziner (2012). They found that the spanwise distortions of streaks caused by oscillatory wall motion disrupt the wall-normal momentum exchange.

Apart from the aforementioned literature on turbulent flow over vibrating bodies, the influences of wall vibration on the growth of perturbations in pre-transitional boundary layer have been studied more recently. Hack & Zaki (2014, 2015) showed that in flow over a spanwise vibrating wall, streaks are weakened because the lift-up effect is hindered in the boundary layer and subsequently the transition to turbulence was delayed. Performing a non-modal stability analysis, the same authors concluded that the weakening effect can be further attributed to the formation of a pressure field redistributing energy from wall-normal to spanwise velocity perturbations. Similar weakening of the lift-up has been reported by Ricco (2011) by examining the amplification of streaks under steady spanwise wall forcing. In addition to the lift-up weakening effect, vibration of the wall also introduces an inviscid cross-flow-type instability, which is related to the inflection points in the spanwise velocity profile. This type of instability overwhelms the lift-up mechanism and promotes transition at high amplitudes of wall vibration (Hack & Zaki 2015). It is also noted that the spanwise vibration frequency affects the thickness of the Stokes layer and an acceleration of transition was observed at small forcing frequencies (Hack & Zaki 2014).

As reviewed previously, most of the work on boundary-layer flow over vibrating surfaces focus on the spanwise wall vibration. The effects of vertical wall vibration on the development of free-steam perturbations, bypass transition and turbulence in

boundary-layer flow are still unclear, even if this fundamental problem resides in a large number of practical cases such as flow around vibrating wings, turbine blades and bridges. On the other hand, vertical forcing introduced on the wall surface has been investigated extensively, but most of them focused on wall blowing or suction (Choi, Moin & Kim 1994; Fransson & Alfredsson 2003; Pamiès *et al.* 2007; Kametani & Fukagata 2011; Xiao & Papadakis 2019). Such forcing was found to be able to offset the wall-normal velocity, thus counteracting the motion of streamwise vortices (Choi *et al.* 1994).

When the leading edge is taken into consideration, the vertical vibration of wall introduces time-dependent angle of attack, which affects the pressure gradient on wall and the curvature of streamlines near the leading edge (similar to the case of pitching airfoil). The streamwise pressure gradient in boundary layer has been shown to have key effects on the growth of perturbations (Zaki & Durbin 2006), whereas the curvature of streamlines tilts and stretches the free-stream vorticity at leading edge to generate streamwise vorticity and subsequently streaks (Schrader *et al.* 2010). In the study of leading edge receptivity to sound, it has been found that when the incidence angle is 15°, the receptivity coefficient is more than three times larger than that in the symmetric case (Hammerton & Kerschen 1996; Fuciarelli, Reed & Lyttle 2000).

1.3. *Motivation*

As presented previously, the vibration of a solid body imposes prominent effects on the flow around it by altering the stability of the fluid–structure system, perturbation development, laminar–turbulent transition, etc. These findings suggest that the vertical vibration of the plate can affect the growth of disturbances inside the boundary layer and change the process of bypass transition. This is a critical problem when modelling or simulating the bypass transition in engineering applications (e.g. predicting the transition point in flow around a vibrating wing) but has not been studied in previous research. Therefore, the present work has been motivated to address: (i) how the vertical vibration affects the linear lift-up mechanism, the generation of streaks induced by free-stream disturbance and the shear sheltering of the boundary layer to high-frequency perturbations; (ii) if the inflow perturbation developments resonate with the wall vibration; (iii) how the vibration affects the nonlinear deformation and secondary instability of streaks and the bypass transition.

In the following, the theoretical formulation is given in § 2, followed by the computational set-up in § 3; the results from linear perturbation analyses are detailed in § 4; the nonlinear response of the boundary-layer is reported in § 5; the final conclusions are drawn in § 6.

2. Governing equations and numerical algorithms

An incompressible flow with free-stream velocity U_∞ over a flat plate with half thickness R is considered and all the following variables are non-dimensionalized by U_∞ and R. In the inertial Cartesian coordinate system, $\tilde{\boldsymbol{x}} = (\tilde{x}, \tilde{y}, \tilde{z})^{\mathrm{T}}$ represents the streamwise, vertical and spanwise directions, respectively and the plate vibrates in the vertical direction with a velocity

$$\boldsymbol{v}_w = (0, A\sin(\omega_w t + \phi), 0)^{\mathrm{T}}, \tag{2.1}$$

where A, ω_w and ϕ are the magnitude, frequency and phase of the vibration, respectively.

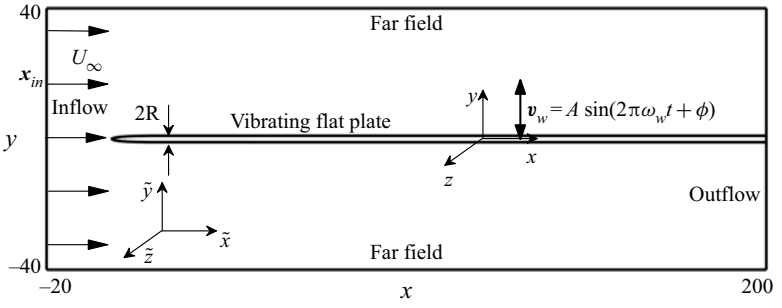

FIGURE 1. Schematic diagram of the computation domain, boundary conditions and the coordinate frameworks.

In the rest of this paper, we adopt a body coordinate system attached to the plate denoted as $\boldsymbol{x} = (x, y, z)^{\mathrm{T}}$ (see figure 1). The variables in the body framework satisfy

$$\boldsymbol{x} + \int_0^t \boldsymbol{v}_w \,\mathrm{d}t = \tilde{\boldsymbol{x}}, \tag{2.2a}$$

$$p = \tilde{p}, \tag{2.2b}$$

$$\boldsymbol{u} + \boldsymbol{v}_w = \tilde{\boldsymbol{u}}, \tag{2.2c}$$

where $\boldsymbol{u} = (u, v, w)^{\mathrm{T}}$ and p are the velocity and pressure of the fluid in the body framework $\boldsymbol{x}$, respectively; and $\tilde{\boldsymbol{u}}$ and $\tilde{p}$ are the velocity and pressure in the inertia framework $\tilde{\boldsymbol{x}}$, respectively.

Then $\boldsymbol{u}$ and p are solutions of the incompressible Navier–Stokes (NS) equations expressed in the body framework:

$$\partial_t \boldsymbol{u} + \boldsymbol{u}\cdot\nabla\boldsymbol{u} + \nabla p - Re^{-1}\nabla^2\boldsymbol{u} + \partial_t \boldsymbol{v}_w + \boldsymbol{v}_w\cdot\nabla\boldsymbol{u} = 0, \tag{2.3a}$$

$$\nabla\cdot\boldsymbol{u} = 0, \tag{2.3b}$$

where Re is the Reynolds number based on U_∞ and R. The last two terms on the left-hand side of (2.3*a*) are non-inertial terms induced by the vibration.

The velocity vector and the pressure can be decomposed as the sum of a base state $(\boldsymbol{U}, P)$ and a perturbation state $(\boldsymbol{u}', p')$, $(\boldsymbol{u}, p) = (\boldsymbol{U}, P) + (\boldsymbol{u}', p')$. When the amplitude of the perturbation is sufficiently small, the development of perturbations can be described by the linearized NS equations

$$\partial_t \boldsymbol{u}' + \boldsymbol{U}\cdot\nabla\boldsymbol{u}' + \boldsymbol{v}_w\cdot\nabla\boldsymbol{u}' + \boldsymbol{u}'\cdot\nabla\boldsymbol{U} + \nabla p' - Re^{-1}\nabla^2\boldsymbol{u}' = 0, \tag{2.4a}$$

$$\nabla\cdot\boldsymbol{u}' = 0, \tag{2.4b}$$

which can be written compactly as $\partial_t\boldsymbol{u}' - \mathcal{L}(\boldsymbol{u}') = 0$ with $\mathcal{L}$ denoting a linear operator depending on the base state.

To study the effects of free-stream disturbance on bypass transition, perturbations are introduced into the domain from the inflow boundary in the form of the velocity boundary condition of (2.4), and the initial condition of $\boldsymbol{u}'$ is set to zero. This inflow perturbation is a function of both space and time and can be decomposed as

$$\boldsymbol{u}'(\boldsymbol{x}_{in}, t) = G(t)\boldsymbol{u}'_{in}(\boldsymbol{x}_{in}), \tag{2.5}$$

where $\boldsymbol{u}'_{in}(\boldsymbol{x}_{in})$ is the spatial dependence of the perturbation, $\boldsymbol{x}_{in}$ denotes the inflow boundary and $G(t)$ is a prescribed temporal function given by $(1 - \mathrm{e}^{-100t^2})$

$(1 - \mathrm{e}^{-100(T_o-t)^2})\mathrm{e}^{\mathrm{i}\omega t}$ in which the first and second terms ensure that the initial condition and boundary condition are compatible (Mao, Blackburn & Sherwin 2013), and ω specifies the frequency of the inflow perturbation.

The amplification of the inflow perturbation in the boundary-layer flow can be described by

$$K(T_o) = \frac{\displaystyle\int_{\Omega} \boldsymbol{u}'(T_o) \cdot \boldsymbol{u}'(T_o) \mathrm{d}\Omega}{\displaystyle\int_{\boldsymbol{x}_{in}} \boldsymbol{u}'_{in} \cdot \boldsymbol{u}'_{in} \, \mathrm{d}S}, \tag{2.6}$$

where Ω represents the upper half of the fluid domain and T_o is the final time. Unless otherwise stated, T_o is set to 180 in this work, as applied by Wang *et al.* (2019). The lower half is symmetric with the upper half and this definition of K takes into account the perturbation amplifications over the upper half only so as to concentrate the resolution on the upper boundary layer.

To quantify the impact of the wall vibration on the inflow perturbation developments, we compare the maximum value of K, denoted as K_{max}, for the vibrating and non-vibrating cases. Clearly this will result in a more robust evaluation of the vibration effect than adopting a random inflow noise. The optimal perturbation is regarded as the most critical component in the broadband free-stream disturbance. The consideration of optimal perturbation highlights the influence of vertical vibration of the wall on the variation and evolution of the key component of broadband disturbance. To compute this optimal value and the corresponding inflow perturbation, we define a Lagrangian functional:

$$L = K(T_o) - \frac{1}{T_o} \int_0^{T_o} \int_{\Omega} [\boldsymbol{u}^{\dagger} \cdot (\partial_t \boldsymbol{u}' - \mathcal{L}(\boldsymbol{u}')] \, \mathrm{d}\Omega \, \mathrm{d}t, \tag{2.7}$$

where $\boldsymbol{u}^{\dagger}$ is the adjoint velocity, the first term on the right-hand side is the objective function to be maximized and the second represents a constraint that the perturbation satisfies the governing equations (2.4). Setting the variations of the Lagrangian functional to zero and after integration by parts, a set of adjoint equation is obtained,

$$\partial_t \boldsymbol{u}^{\dagger} + (\boldsymbol{U} + \boldsymbol{v}_w) \cdot \nabla \boldsymbol{u}^{\dagger} - \nabla \boldsymbol{U} \cdot \boldsymbol{u}^{\dagger} - \nabla p^{\dagger} + Re^{-1} \nabla^2 \boldsymbol{u}^{\dagger} = 0, \tag{2.8a}$$

$$\nabla \cdot \boldsymbol{u}^{\dagger} = 0, \tag{2.8b}$$

where $p^{\dagger}$ is the adjoint pressure and the initial condition for the adjoint velocity is given by

$$\boldsymbol{u}^{\dagger}(T_o) = \frac{2\boldsymbol{u}'(T_o)}{\displaystyle\int_{\boldsymbol{x}_{in}} \boldsymbol{u}'_{in} \cdot \boldsymbol{u}'_{in} \, \mathrm{d}S}. \tag{2.9}$$

The gradient of the Lagrangian functional with respect to the inflow perturbation is given by

$$\nabla_{\boldsymbol{u}'_{in}} L = \frac{-2 \displaystyle\int_{\Omega} \boldsymbol{u}'(T_o) \cdot \boldsymbol{u}'(T_o) \mathrm{d}\Omega}{\left(\displaystyle\int_{\boldsymbol{x}_{in}} \boldsymbol{u}'_{in} \cdot \boldsymbol{u}'_{in} \, \mathrm{d}S \right)^2} \boldsymbol{u}'_{in} + \frac{1}{T_o} \int_0^{T_o} (p^{\dagger} \boldsymbol{n} - Re^{-1} \nabla_{\boldsymbol{n}} \boldsymbol{u}^{\dagger}) G \, \mathrm{d}t, \tag{2.10}$$

where $\boldsymbol{n}$ is the unit outward norm of the inflow boundary.

Boundary	Conditions for $\boldsymbol{u}$	$\boldsymbol{u}'$	$\boldsymbol{u}^\dagger$
Inflow	$\boldsymbol{u} = (1, -A\sin(\omega_w t + \phi), 0)^{\mathrm{T}}$	$\boldsymbol{u}' = (0, 0, 0)^{\mathrm{T}}$	$\boldsymbol{u}^\dagger = (0, 0, 0)^{\mathrm{T}}$
Outflow	$\nabla_n \boldsymbol{u} = 0$	$\boldsymbol{u}' = (0, 0, 0)^{\mathrm{T}}$	$Re^{-1}\boldsymbol{n}\cdot\nabla\boldsymbol{u}^\dagger + \boldsymbol{n}\cdot\boldsymbol{U}\boldsymbol{u}^\dagger = 0$
Far-field	$\partial u/\partial y = 0, \partial w/\partial y = 0,$ $v = -A\sin(\omega_w t + \phi)$	$\boldsymbol{u}' = (0, 0, 0)^{\mathrm{T}}$	$\boldsymbol{u}^\dagger = (0, 0, 0)^{\mathrm{T}}$
Flat plate	$\boldsymbol{u} = (0, 0, 0)^{\mathrm{T}}$	$\boldsymbol{u}' = (0, 0, 0)^{\mathrm{T}}$	$\boldsymbol{u}^\dagger = (0, 0, 0)^{\mathrm{T}}$

TABLE 1. Summary of boundary conditions.

A gradient-based iterative optimization algorithm is used to find the optimal inflow perturbation. When the gradient of the Lagrangian with respect to the inflow perturbation vanishes, the obtained inflow perturbation is the optimal one generating the most energetic perturbations in the boundary-layer flow, and the corresponding K takes the maximum value K_{max}. Further details of the algorithm can be found in Mao *et al.* (2013).

3. Computation set-up

The computation domain is shown in figure 1. The inflow boundary locates at $x = -20$ and the outflow boundary is at $x = 200$. In the wall-normal direction, the domain spans from $y = -40$ to $y = 40$. The leading edge of the two-dimensional (2-D) plate is located at $(0, 0, 0)^{\mathrm{T}}$. The streamwise length of the plate is $l = 200$ for most of the studies and is extended to 300 for the investigation of transition, and its half-thickness is used as the characteristic length. In the spanwise direction, a complex Fourier decomposition is applied to the perturbation velocity:

$$\boldsymbol{u}'(x, y, z) = \sum_{\beta=0}^{\infty} \boldsymbol{u}'_\beta(x, y)\mathrm{e}^{\mathrm{i}\beta z}. \tag{3.1}$$

The base flow is a 2-D solution of the NS equations (2.3). It is unsteady owing to the periodic vibration of the plate and snapshots of the velocity field are saved after reaching a periodic state when solving the 2-D NS equations. A Lagrangian interpolation is used to reconstruct the base flow U at every time step when solving (2.4) and (2.8) (Mao, Sherwin & Blackburn 2011). In the linear regime, perturbations with different spanwise wavenumbers are decoupled and can be simulated independently. A spectral element method is used to discretize the governing equations in the x–y plane (Karniadakis & Sherwin 2007). In this work, the domain is decomposed into 3835 elements and each element is further decomposed into a $(N + 1)(N + 1)$ grid, where N represents the polynomial order of the spectral discretization.

A summary of boundary conditions is given in table 1. Zero-Neumann boundary conditions are used for the pressure term on all boundaries, except for the outflow boundary, where the pressure is set to zero. The boundary conditions for the adjoint variables ensure that the variances of the Lagrangian functional are zero (Blackburn & Sherwin 2004; Mao *et al.* 2013).

The convergence tests for grid resolution are conducted by varying the polynomial order N in each element in the x–y plane. The resolution in the spanwise direction is only relevant to three-dimensional (3-D) studies and is presented in § 5. Figure 2 shows the convergence of K_{max} at $\beta = 1.4$ and $Re = 800$, the largest Reynolds number considered in

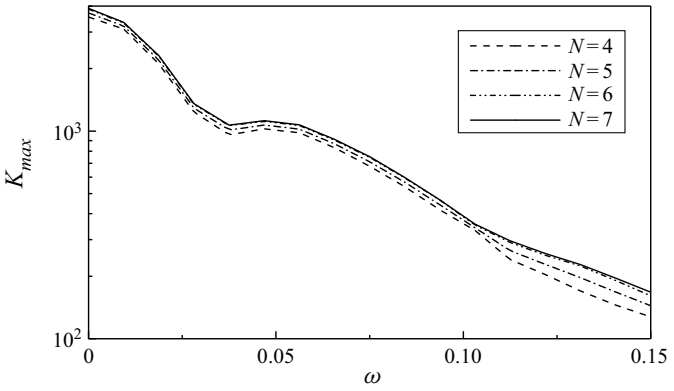

FIGURE 2. Convergence of K_{max} with respect to the polynomial order N at $(Re, \beta) = (800, 1.4)$, and various ω.

this work. At $N = 7$, the optimal gain K_{max} converges to three significant digits and this polynomial order will be used in all the following linear and nonlinear calculations.

4. Linear perturbation analyses

Adopting the algorithms presented in § 2, we conduct the linear perturbation analyses to investigate the development of the optimal inflow perturbations over the vibrating plate. First, the base flow around the vibrating flat plate is presented.

4.1. *The base flow*

The base flow obtained by integrating (2.3) over enough cycles of the plate vibration until reaching periodic states at $Re = 800$, $A = 0.01$ and $\omega_w = 2\pi/180$ is shown in figure 3. Here the phase of vibration ϕ only shifts the initial phase of the base flow. Without loss of generality, $\phi = 0$ is adopted. Later in § 4.3, effects of ϕ are discussed. The vibration leads to a sinusoidal variation of the angle of attack, which can be visualized from the instantaneous flow fields at different phases as shown in figure 3(*a*,*b*). In figure 3(*c*), the mean velocity averaged over a period for the vibrating plate almost overlaps with the steady velocity profile for a fixed plate and the Blasius solution, indicating that the plate vibration does not change the mean boundary-layer profile over the parameters studied. It is also observed that the instantaneous velocity profile remains Blasius-like and shifts around the steady solution. The evolution of the boundary-layer thickness δ, which reaches $\delta = 2.27R$ at $x = 200$, also shows that the small vertical vibration in this study has little effect on the mean boundary-layer flow (see figure 3*e*). As the pressure on the windward side is larger than that on the leeward side, pressure on the upper surface increases or decreases from the mean value when the plate is moving upward or downward (see figure 3*d*) and the largest variance can be found around the leading edge. We show the pressure distribution along the upper surface, while a similar pressure field is developed on the lower surface and is not presented here. The flow is therefore subject to alternating favourable and adverse pressure gradients around the leading edge in one vibration cycle. Further downstream of the leading edge, the mean flow undergoes small favourable pressure gradients while instantaneously, negative pressure gradient exists over almost half of the cycle. Though the vibration amplitude of the plate is small, it produces remarkable change of flow with time. Base flows at other Re, A and ω_w considered in this work are also featured by sinusoidally

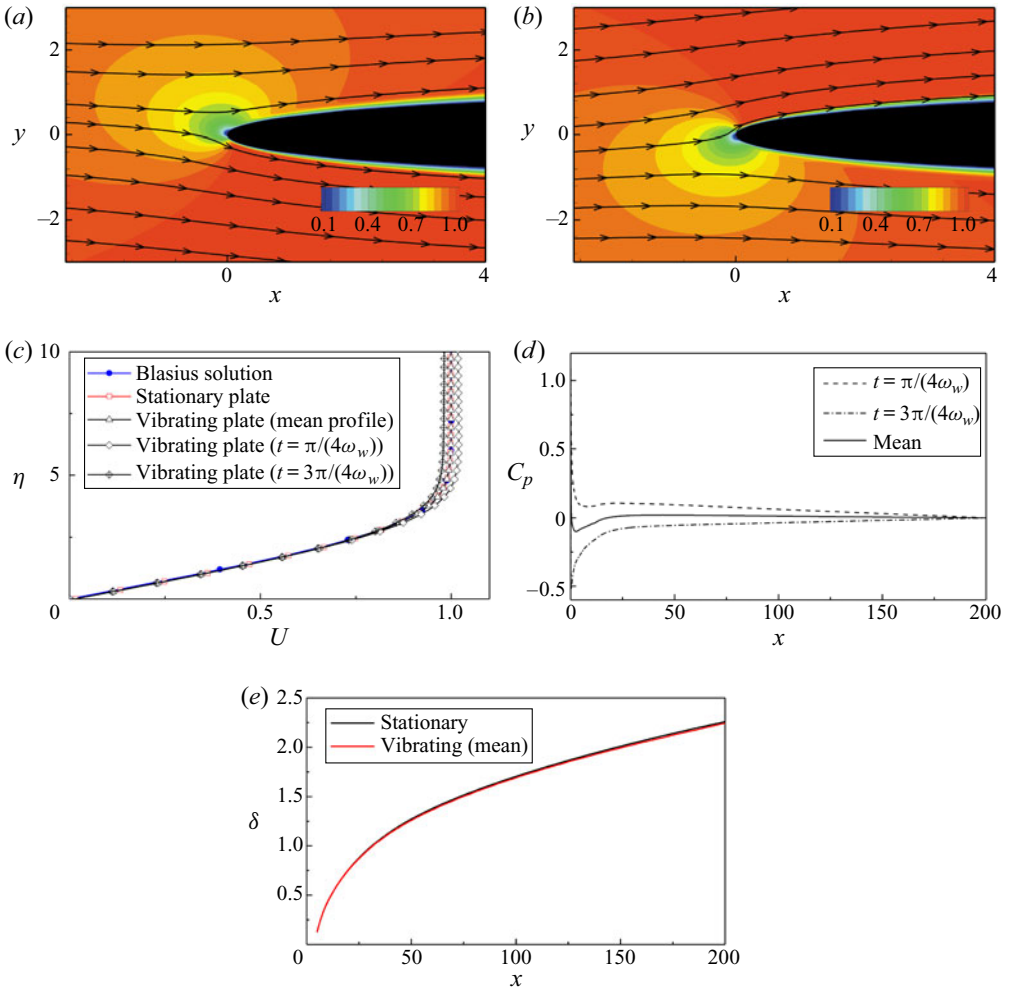

FIGURE 3. Base flow at $(Re, A, \omega_w) = (800, 0.01, 2\pi/180)$. (*a*), (*b*) Contours of streamwise velocity and streamlines around the leading edge at $t = \pi/(4\omega_w)$ and $t = 3\pi/(4\omega_w)$, respectively. (*c*) Comparisons of velocity profiles at $x = 100$, η is defined as $y/\sqrt{Re \cdot x}$. (*d*) Pressure coefficient $C_p = p - p_\infty$, where p_∞ is the non-dimensionalized pressure in the far field, along the upper surface of the plate. (*e*) Development of the boundary-layer thickness along the flat plate.

varying angles of attack and time-dependent pressure gradients, and are not shown here for brevity.

4.2. *Amplification of inflow perturbations*

The optimal inflow perturbations and the gain K_{max} are then calculated following the algorithms outlined in § 2. It is noted that if the plate does not vibrate, the linear dynamics can be further simplified by studying only the half of the domain with symmetric/asymmetric boundary conditions at $y = 0$ (Wang *et al.* 2019). However, in the present investigation, the full domain is considered to accommodate the vibration effect, even if the resolution is concentrated on the upper half.

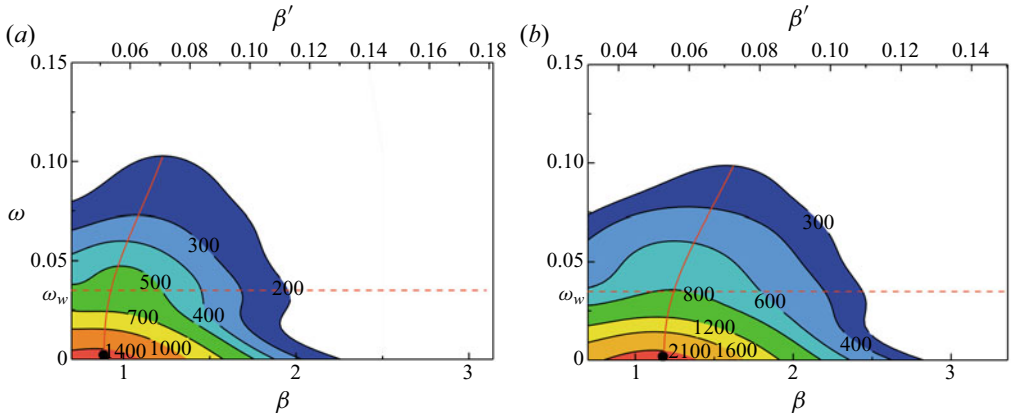

FIGURE 4. Contours of K_{max} for optimal inflow perturbations at $(\omega_w, A) = (2\pi/180, 0.01)$ with (*a*) $Re = 300$ and (*b*) $Re = 500$. The red dashed line marks the vibration frequency of the flat plate and the red solid line illustrates the optimal spanwise wavenumber at different ω. The black circle represents the global maximum point of K_{max}. Here β' is a normalized spanwise wavenumber.

Effects of the Reynolds number on the optimal gain K_{max} are shown in figure 4, where the contours of K_{max} over a wide range of spanwise wavenumbers and perturbation frequencies are compared.Over the Reynolds numbers considered, the global maximum of K_{max} across the range of β and ω studied corresponds to the steady inflow perturbation, similar to the result for a fixed plate (Monokrousos *et al.* 2010). As the Reynolds number increases from $Re = 300$ to $Re = 500$ and $Re = 800$ (figures 4*a*,*b* and 6*c*), the boundary layer's response to disturbances becomes more energetic, and the optimal spanwise wavenumber at which the gain of the steady perturbation reaches maximum increases from 0.87 to 1.14 and 1.4, respectively. By taking into account the normalized wavenumber,

$$\beta' = \beta/\sqrt{Re}, \tag{4.1}$$

the three Reynolds numbers give rise to optimal wavenumbers $\beta'_{max} = \{4.95, 5.10, 5.02\} \times 10^{-2}$, indicating that the optimal spanwise wavenumber at $\omega = 0$ is insensitive to Re after the appropriate normalization (Luchini 2000; Andersson *et al.* 2001).

Actually, the optimal spanwise wavenumbers at other perturbation frequencies are also insensitive to the Reynolds number. The red solid curves in figure 4, which connect the optimal spanwise wavenumber at different perturbation frequencies, are extracted and plotted compactly in figure 5. With the same vibration frequency and amplitude, the curves at different Reynolds numbers show a similar shape. The optimal spanwise wavenumber increases slowly when ω is small and then rises almost linearly for larger ω. Over the range of perturbation frequencies considered ($\omega < 0.15$), the curves can be fitted as the Logistic functions, which can be approximately unified as $\omega = C_2 + (C_1 - C_2)/(1 + (\beta'_{max}/C_3)^{\sigma})$, where $C_1 = 0.0508$, $C_2 = 0.0975$, $C_3 = 0.122$ and $\sigma = 2.39$ for the present case. Later, we show that this Re insensitive parameter β'_{max} strongly depends on the vibration of the plate. From figures 4 and 6(*c*), we also find that the optimal gain K_{max} decreases with ω, manifesting the shear sheltering mechanism of the boundary layer to high-frequency disturbances. As shown later, this nearly monotonic decrease does not hold when the plate vibrates at high frequencies. After clarifying the Reynolds number effects, we focus on $Re = 800$ in the following analyses.

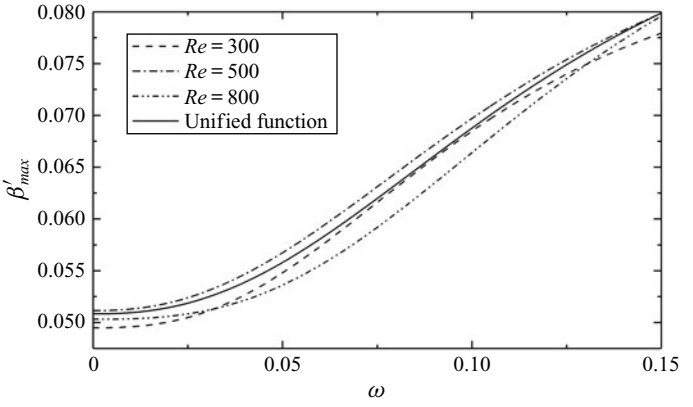

FIGURE 5. Variation of the optimal spanwise wavenumber at different Reynolds numbers.

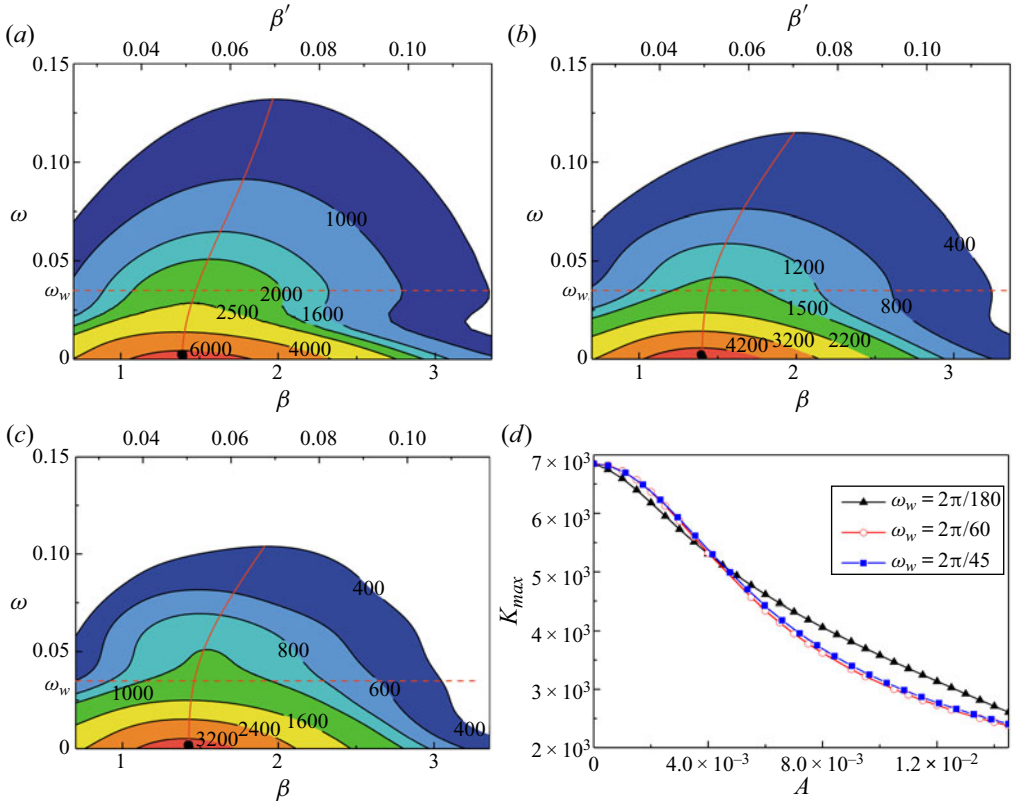

FIGURE 6. Effects of vibration amplitude on the amplification of the optimal inflow perturbations. (*a*) Contours of K_{max} at $(Re, \omega_w, A) = (800, 2\pi/180, 0)$. (*b*) Contours of K_{max} at $(Re, \omega_w, A) = (800, 2\pi/180, 0.005)$. (*c*) Contours of K_{max} at $(Re, \omega_w, A) = (800, 2\pi/180, 0.01)$. (*d*) Variation of the global maximum of K_{max} with vibration amplitude A. In contours (*a*) to (*c*), the red dashed line marks the vibration frequency of the flat plate and the red solid line connects the optimal spanwise wavenumbers at different ω. The black circle represents the point of the global maximum of K_{max}.

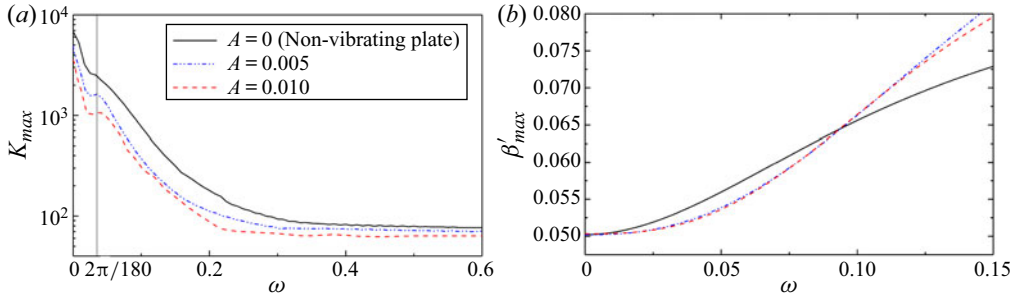

FIGURE 7. Effects of vibration amplitude on the cut-off frequency and optimal spanwise wavenumber. (*a*) Variation of K_{max} with ω at $(Re, \beta) = (800, 1.4)$. The vertical lines denote the position of $\omega = \omega_w = 2\pi/180$. (*b*) Variation of β'_{max} with ω.

The influences of vibration amplitudes on the amplification of optimal inflow perturbations are presented in figure 6. Under the range of parameters considered, a stronger vibration results in weaker amplification of the inflow perturbations. The global maximum of K_{max}, which is obtained at spanwise wavenumber $\beta = 1.4$ and frequency $\omega = 0$, decreases from 6850 to 4936 and 3580 when the vibration amplitude increases from 0 (non-vibrating) to 0.005 and 0.01, as shown in figure 6(*a–c*). The variation of the global maximum of K_{max} with the vibration amplitude at given frequencies is shown in figure 6(*d*). It confirms that the global maximum amplification of the inflow perturbation decreases monotonically with the vibration amplitude A. Compared with the fixed plate case, the reduction of the global maximum gain is up to 60 % at $A = 0.0145$, suggesting that the lift-up mechanism would be suppressed owing to the plate vibration.

The amplification of optimal inflow perturbations at $\beta = 1.4$ for different vibration amplitudes is extracted and presented in figure 7(*a*). It shows that the amplification of the optimal perturbation reduces faster as ω increases for higher vibration amplitudes. Above a critical frequency, the inflow perturbation does not enter the boundary layer and develops in the free stream. If ignoring the viscous diffusion, the corresponding perturbation growth is $K_{max} = To/2 = 90$. This critical frequency is defined as the cut-off frequency, which decreases with the vibration amplitude A as can be seen in figure 7(*a*). This observation suggests that the vibration strengthens the sheltering effect of the boundary layer to high-frequency free-stream disturbance (it will be shown later that this is true only at low vibration frequencies). In addition to the cut-off frequency, the vibration also clearly alters the optimal spanwise wavenumber (see figure 7*b*), which has been shown to be insensitive to Re in figure 5.

The contour maps of K_{max} for different vibration frequencies are presented in figures 6(*c*), 8(*a*) and 8(*b*). The global maximum of K_{max} decreases as the vibration frequency ω_w increases. Compared with low-frequency vibration cases (figure 6), the high-frequency vibration of the plate apparently induces a second local peak on the contour plot of K_{max}. The first peak remains at $\omega = 0$ with a reduced value as compared with the stationary plate result, whereas the second appears at $\omega = \omega_w$. This new peak can be considered as a manifestation of the resonance effect of the flow perturbations and the vibrating plate and is the focus of the rest of this work. In fact, there is always a resonance effect as long as the plate vibrates. For the lower-frequency case ($\omega_w = 2\pi/180$ in figure 6*b*,*c*), the resonance peak is submerged in the main contour so it is not clearly visible. Figure 7(*a*) shows that the curves of K_{max} present a small local peak at $\omega = \omega_w = 2\pi/180$, manifesting a weak resonance effect for a low-frequency

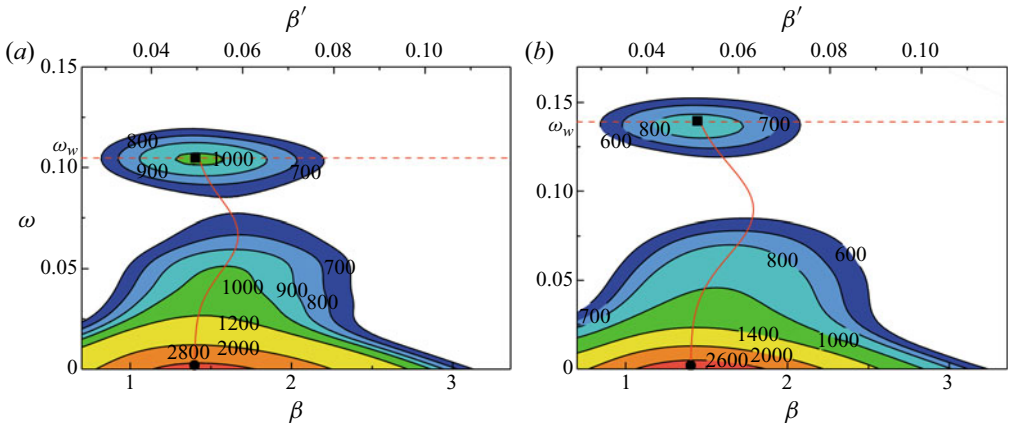

FIGURE 8. Effect of vibration frequency on the amplification of optimal inflow perturbations. (*a*) Contours of K_{max} at $(Re, \omega_w, A) = (800, 2\pi/60, 0.01)$. (*b*) Contours of K_{max} at $(Re, \omega_w, A) = (800, 2\pi/45, 0.01)$. The red dashed line marks the vibration frequency of the flat plate and the red solid line connects the optimal spanwise wavenumbers at different ω. The black circle represents the point of local maximum of K_{max}. The black square point marks the resonant point.

vibrating plate. The profile of the normalized optimal spanwise wavenumber (marked by the red line in figure 8) shows that the optimal β increases and then decreases with ω when there is a resonance induced local maximum of perturbation amplification. At the resonant frequency, the optimal spanwise wavenumber equals that at zero perturbation frequency ($\beta = 1.4$), indicating a similar mechanism of perturbation amplifications (and streak generations) at the resonance frequency and zero perturbation frequency. This will be further illustrated in § 4.3. To summarize, a higher magnitude of the plate vibration results in a lower perturbation amplification and lower cut-off frequency, whereas a higher vibrating frequency results in clear resonance with the perturbation development.

4.3. *Resonance between the vibrating plate and perturbations*

The details of the influences of resonance on the perturbation amplifications are plotted in figure 9. The amplification of the optimal inflow perturbations shows a downward trend owing to the shielding mechanism of the boundary layer, as can be seen in figure 9. Further, K_{max} fluctuates owing to the plate vibration and several peak values (marked by solid dots) appear at the harmonics of ω_w, manifesting the resonance phenomena. Therefore, the curves can be interpreted as the superposed effects of the boundary-layer sheltering to high-frequency perturbations and resonance between perturbations and the plate. One of the consequences is that the cut-off frequency becomes higher when resonance happens, indicating that higher-frequency free-stream perturbations are admitted by the boundary layer owing to the plate vibration. Within the scope of parameters considered, the resonance-induced gain is still smaller than that at zero frequency. For example, the gain at $\omega = \omega_w = 2\pi/60$ is about 36 % of the gain at $\omega = 0$. We focus on the resonance-induced gain because it allows higher-frequency perturbations to enter the boundary layer, which might alter the bypass transition process on the vertically vibrating plate. For instance, the resonance-induced gain is 1.46 times of the gain of stationary case at the same perturbation frequency $\omega = 2\pi/60$.

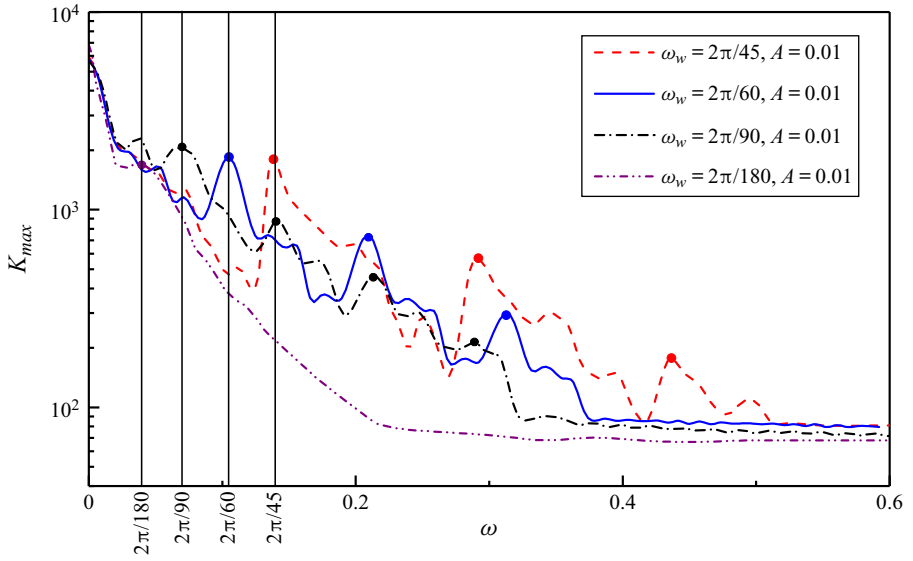

FIGURE 9. Variation of K_{max} with ω at $(Re, \beta) = (800, 1.4)$ for different ω_w. The dots denote the resonant points. The vertical lines denote the position of $\omega = \omega_w$.

To further examine the resonance effect, the velocity profiles of the optimal inflow perturbation at various ω_w are shown in figure 10. The inflow perturbations are scaled so that they have the same energy or norm, which is defined as

$$\|\boldsymbol{u}'_{in}\| = \sqrt{\int_{\boldsymbol{x}_{in}} \boldsymbol{u}'_{in} \cdot \boldsymbol{u}'_{in} \, \mathrm{d}S}. \tag{4.2}$$

As the velocity is optimized to induce maximum perturbation gain on the upper half of the domain, the perturbation velocity reduces to trivial levels for $y > 5$ or $y < -1$. The inflow velocity perturbation is decomposed into streamwise (u'), wall-normal (v') and spanwise (w') components. The velocity profiles show that the optimal perturbations are mainly composed of wall-normal and spanwise components, although there is a weak streamwise one (see figure 10*a*,*b*). The streamwise vorticity perturbation formed by the wall-normal and spanwise components tilts the base shear profile and leads to the generation of streamwise perturbation via the lift-up mechanism. Therefore, if there is no leading edge, the optimal inflow velocity should be concentrated on the wall-normal and spanwise components only. However, the leading edge tilts the inflow perturbations and therefore a streamwise velocity perturbation component appears in the optimal profile and will contribute to the streamwise vorticity downstream of the leading edge (Wanderley & Corke 2001; Schrader *et al.* 2010). Figure 10(*a*) also shows that the optimal disturbance of the stationary case is concentrated at $0 < y < 2$ and associated with the boundary layer on the upper surface. As a result of the vertical vibration of the wall, the optimal perturbation of the vibrating case is less localized as compared with that of the stationary case (see figure 10*d*). In the resonance regime, the velocity profile over the vibrating plate consists of more layers in the vertical direction than that over the stationary plate, as shown in figure 10(*b*,*e*). This multi-layer structure will be shown later to be critical to activate the resonance. Above the cut-off frequency, the velocity profiles in figure 10(*c*,*f*) share similar shapes. The wall-normal component (v') is small whereas u' becomes the dominant

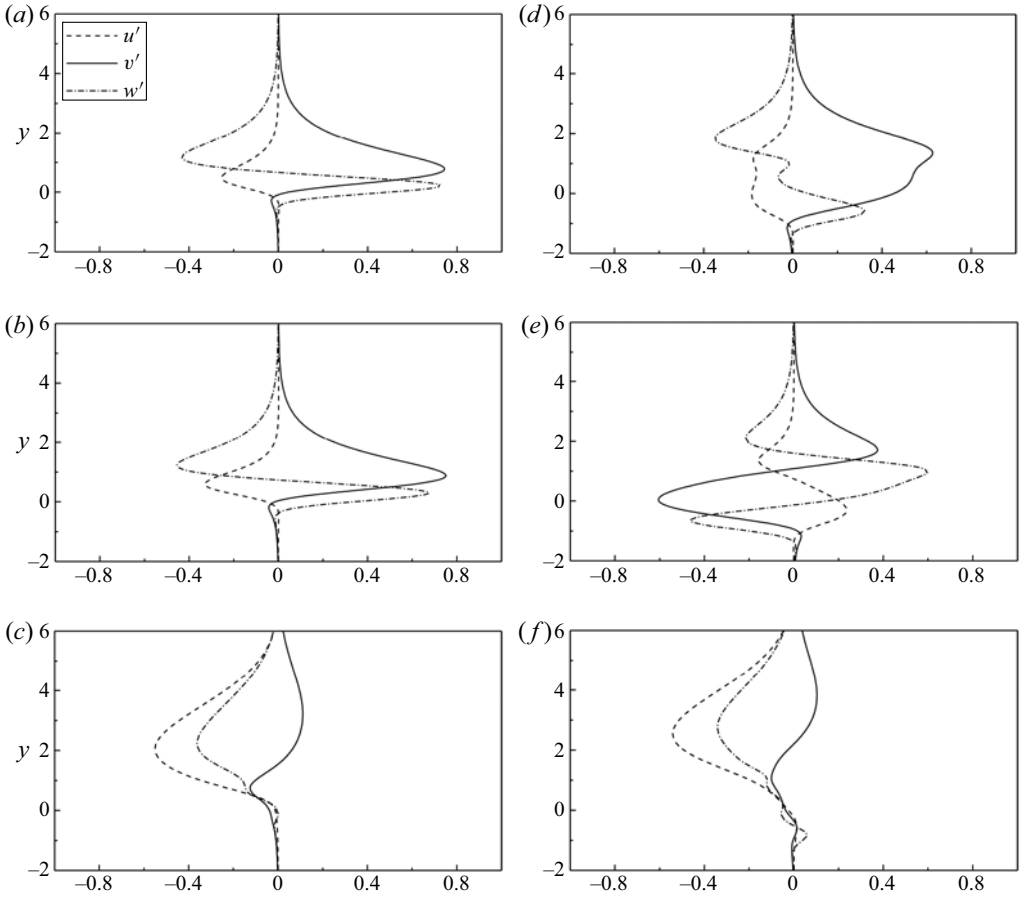

FIGURE 10. Velocity profile of the optimal inflow perturbation at $(Re, \beta) = (800, 1.4)$: (a), (b) and (c) perturbation components for a non-vibrating plate at $\omega = 0$, $\omega = 2\pi/60$ and $\omega = 0.5$, respectively; (d)–(f) same parameters as (a)–(c) but for the vibrating plate with $\omega_w = 2\pi/60$.

component, which can be attributed to the ineffective lift-up mechanism above the cut-off frequency.

In figure 11, we further acquire the responses of the boundary-layer flow to the optimal inflow perturbations by applying the optimal perturbations at the inflow and integrating the linearized NS equations (2.4). Again, the inflow perturbations are normalized to have a unit norm. As mentioned previously, the steady inflow perturbations penetrate the boundary layer and activate the lift-up mechanism to generate elongated streamwise velocity streaks in the boundary layer while the plate vibration reduces the magnitude of the streaks as can be inferred from figure 6. This is confirmed by the streak profiles shown in figure 11(a,b), where the plate is stationary and vibrating, respectively. At $\omega = 2\pi/60$, which is still below the cut-off frequency, short streaks with alternating signs in the streamwise are induced by the optimal inflow perturbation over a stationary plate (see figure 11c). When the plate vibrates and resonance occurs, the sign of the streaks becomes invariant and a single streak is generated (see figure 11d). This effective generation of strong streak reflects the large amplification of the optimal inflow perturbation (shown in figure 10e) illustrated by the local peak of K_{max} in figure 9. The mechanism to generate such elongated streaks will be explored later. The high-frequency perturbations over the cut-off

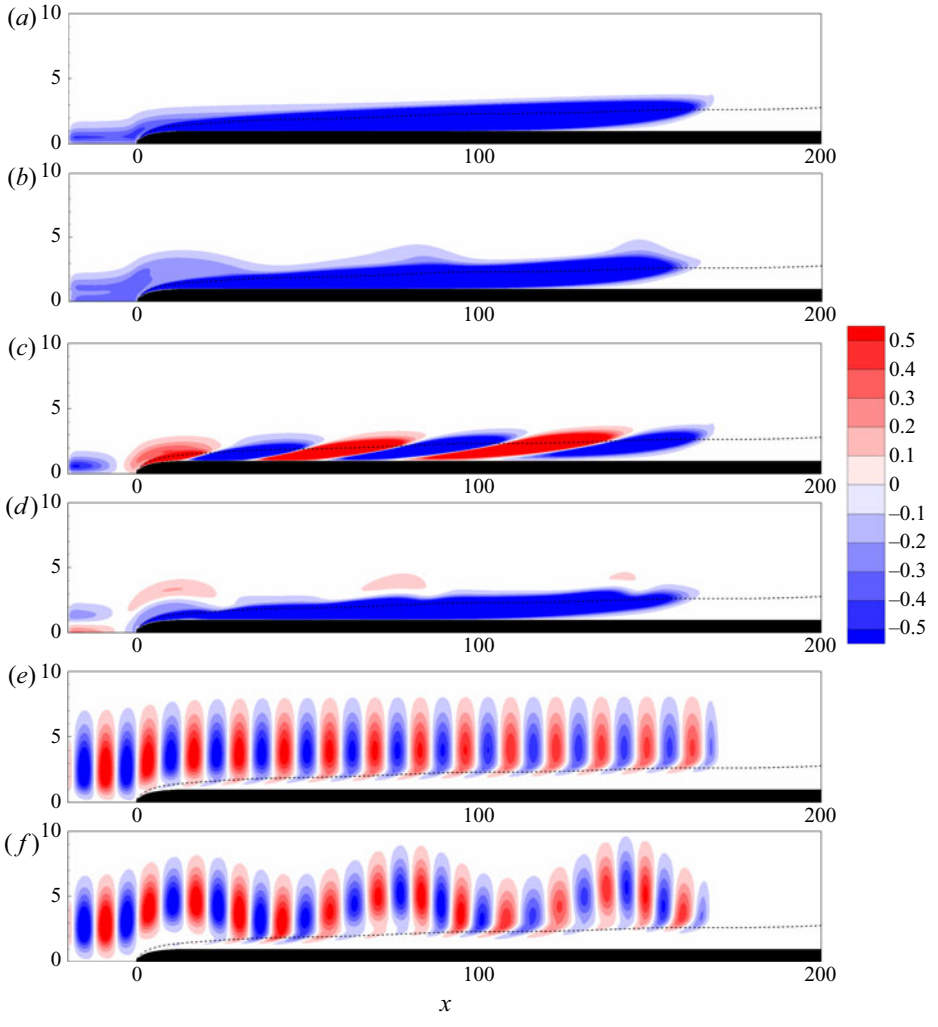

FIGURE 11. Side view of isosurfaces of streamwise perturbation u' at $(Re, t) = (800, 180)$: (a,b) $\omega = 0$; (c,d) $\omega = \omega_w$ and (e,f) $\omega = 0.5$. (a), (c) and (e) Non-vibrating plate and (b), (d) and (f) vibrating plate at $\omega_w = 2\pi/60$. The dashed line marks the boundary-layer thickness δ, which is the height from the wall where the streamwise velocity reaches 99 % of the free-stream velocity.

frequency can hardly penetrate the boundary layer and mainly reside in the free stream while the plate vibration induces the vertical motion of the perturbation (see figure 11e,f). This observation agrees with the shear sheltering effect on high-frequency perturbations revealed by Zaki & Saha (2009). As the responses of the boundary layer to disturbances with frequencies above the cut-off value are weak, such high-frequency optimal inflow perturbations will not be considered further. Please note that we only show the evolution of the optimal perturbations at three perturbation frequencies $\omega = 0, 2\pi/60, 0.5$ in figure 11. In fact, the inflow perturbation with frequency above $\omega = 2\pi/60 \approx 0.105$ is still allowed inside the boundary layer because it is below the cut-off frequency $\omega = 0.37$.

Comparing the present outcome with the case of transversely oscillating wall considered by Hack & Zaki (2012), the transverse oscillation introduces the Stokes shear layer to

the boundary-layer flow, which leads to a substantial reduction of free-stream disturbance energy entering the boundary layer. In addition to the stronger shear sheltering effect, the Stokes shear layer reorients the shear vector and imposes a new restriction on the set of penetrating modes such that the orientation of modes subject to weak sheltering effect deviates from the streamwise direction. For our case of vertically vibrating flat plate, the vibration introduces the periodic variation of the angle of attack, which leads to the time harmonic pressure gradient on the wall. As the vertical vibration in our work is small, this pressure gradient is only significant around the leading edge and becomes negligible on the flat plate far from the leading edge. The shear layer on the vertically vibration wall is thus inappreciably changed by the time harmonic pressure gradient on the plate. However, the shear sheltering of the boundary-layer flow is still influenced by the vertical wall motion because it allows synchronized inflow perturbation entering the boundary layer.

To inspect the effect of plate vibration on the resonance of the fluid flow more closely, the evolution history of the perturbation is shown in figure 12. Note that over the optimization time $T_o = 180$, the inflow perturbation (and the plate vibration) presents three cycles. At $t = 3T_o/12$, the streamwise velocity perturbation upstream of the leading edge consists of a positive and a negative component, matching the profile of the inflow perturbation in figure 10(*e*). Then the free-stream perturbation is stretched and tilted by the curved mean-flow streamlines near the leading edge (see figure 3*a*,*b*). When the inflow disturbance moves closer to the leading edge, the upward/downward movement of the plate imposes a negative/positive angle of attack, which shifts the inflow perturbation towards the lower/upper side of the plate. As a result, the inflow disturbance is staggered. As the frequency and phase the plate vibration and flow oscillation match each other, both the negative and positive components of the streamwise velocity perturbation enter the upper side of the plate and the negative (positive) part is in (out of) the boundary layer at $t = 3T_o/12$. Then at $t = 5T_o/12$, the positive perturbation on the lower array is shifted to the lower side of the plate, while the negative perturbation on the upper array enters into the upper side. In other words, the inflow disturbance is appropriately staggered that only the same sign of perturbation can remain inside the boundary layer. At $t = 7T_o/12$, the negative components of the streamwise velocity on the lower array enters the upper side of the plate again, completing a vibration cycle started at $t = 3T_o/12$. At $t = 9T_o/12$ and $t = 11T_o/12$, as the negative streamwise velocity is continuously convected downstream, an elongated streak is formed on the upper side. The streamwise vorticity shown in the right column of figure 12 presents similar staggered motion as the streamwise velocity. As the sign of the streamwise vorticity inside the upper boundary layer remains the same, it has the capacity to amplify the streaks to a magnitude much larger than the non-resonance cases. At this point of view, the multi-arrays of inflow disturbance is necessary to produce a sign-invariant perturbation inside the boundary layer and thus induce an energetic streaky response, which is exactly the case of optimal inflow perturbation shown in figure 10(*e*). The negative streamwise vorticity on the lower array, which enters into the upper side of the plate due to the downward movement of the plate (see at $t = 3T_o/12, 7T_o/12, 11T_o/12$), is named as ξ'_{x1}. The negative streamwise vorticity on the upper array, which enters into the upper side of the plate because of the upward movement of the plate (see at $t = 5T_o/12, 9T_o/12$), is denoted as ξ'_{x2}. In § 5, we show that ξ'_{x1} and ξ'_{x2} have profound effects on the distortion of low-speed streaks.

The pattern of the staggering, illustrating a synchronization of the motion of the plate and the perturbation, is shown in figure 13, where the black arrows represent the angle of attack as the disturbances move around the leading edge. This effect increases monotonically with the vibration amplitude A. For steady inflow perturbations, the vibrating plate shifts the streamwise vorticity to lower/upper side of the plate when the

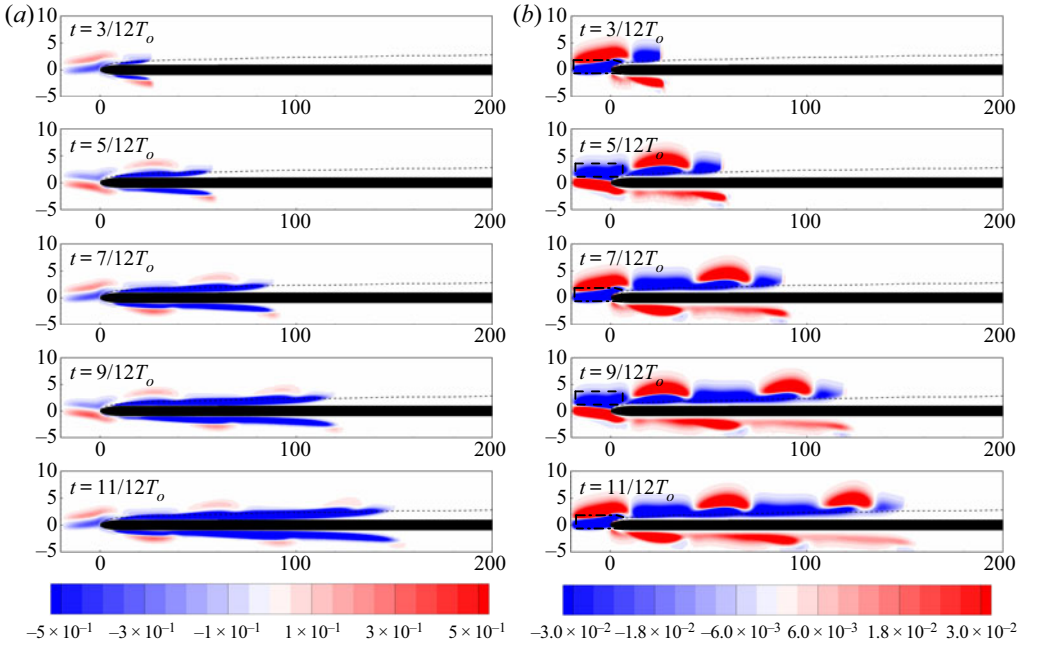

FIGURE 12. Evolution of resonant inflow perturbations (*a*) u' and (*b*) streamwise vorticity ξ_x' at $\omega = \omega_w = 2\pi/60$. The dashed line marks the boundary-layer thickness on the upper side, δ. The dashed box marks the incoming ξ_{x2}' and the dash-dotted box marks the incoming ξ_{x1}'.

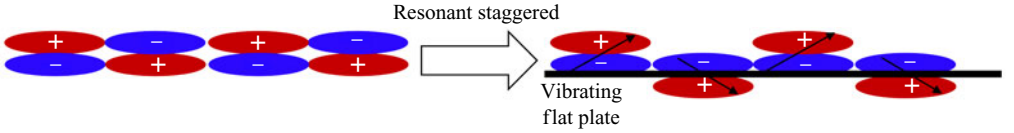

FIGURE 13. Schematic plot of the staggering effect of vibrating plate at resonant frequency. The black arrows represent the angle of attack as the disturbances move around the leading edge.

plate is moving upwards/downwards. Therefore, the free-stream streamwise vorticity and velocity entering the upper side of the boundary layer are broken into segments, preventing the continuous amplification of the streaks, and subsequently the lift-up mechanism is weakened by the plate vibration. As a result, the amplification of steady free-stream perturbations in the boundary layer over a vibrating surface reduces at higher vibration magnitude A as observed in figure 6(*d*). In fact, the synchronization of the motion of the plate and the perturbation can also be activated when the vibration frequency is half of the perturbation frequency. Therefore, there are peaks at $0.5 \times \omega_w$ in figure 9, though the peak values are small.

From the discussion given previously, clearly the resonance depends on the match of frequencies and phases between the vibration and inflow disturbances. When the match is broken, the synchronized staggering disappears and disturbances are disordered on the upper part of the plate. Figure 14 shows the response of boundary-layer under different initial phases of the vibrating plate. The optimal inflow perturbation shown in figure 10(*e*) is applied on the inflow boundary when we integrate the linearized NS equations.

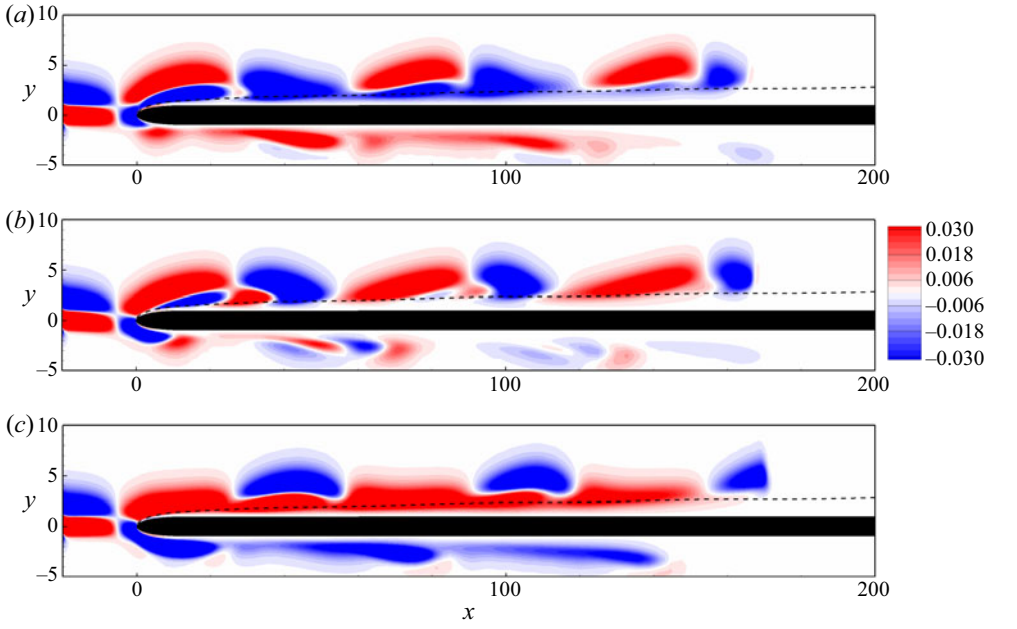

FIGURE 14. Contour of streamwise vorticity ξ_x' under different initial phases (*a*) $\phi = \pi/4$, (*b*) $\phi = \pi/2$ and (*c*) $\phi = \pi$. The optimal inflow perturbation at $(Re, \omega, \omega_w) = (800, 2\pi/60, 2\pi/60)$ is imposed on the inflow. The dashed line marks the boundary-layer thickness, δ.

The perturbation vorticity is tilted more obviously by the leading edge when the initial phase of vibration is $\phi = \pi/4$ (see figure 14*a*), compared with the results shown in figure 12(*b*) when the initial phase is zero. Although the perturbation is more inclined, the streamwise vorticity in the upper boundary layer is still sign-invariant. In fact, the resonance effect is robust and can be found over a wide range of phases (around $\phi = \pm\pi/4$) because the inflow disturbances can tilt and deform to climb over the leading edge. When the phase difference is increased to $\phi = \pi/2$, the perturbation is cut by the vibrating leading edge and tilted severely (see 14*b*). The inflow disturbance is staggered inappropriately at this case and thus both positive and negative streamwise vorticity enter the boundary layer. The opposite phase $\phi = \pi$ gives rise to continuous positive streamwise vorticity inside the boundary-layer because now it is the other array of inflow perturbation that remains inside the boundary layer, which is confirmed by comparing the perturbation around the leading edge (shown in figure 14*c*). It is also worth noting that at those mismatched phases, the inflow perturbation is no longer the optimal solution, while the optimal one ensures a phase match and the synchronized motion by slightly adjusting its frequency around the vibration frequency.

5. Resonance-induced bypass transition

As discussed in the previous linear study, the optimal inflow perturbations in resonance with the vibrating plate produce the elongated, high-amplitude streamwise streaks whose further nonlinear development can be expected to lead to bypass transition as revealed by numerous work in flow around stationary plates. In this section, the 3-D DNS is performed to examine the breakdown of streaks and transition to turbulence activated by the resonant inflow perturbation. The computational domain is extended to $x = 300$ to incorporate the

inception of bypass transition and the spanwise width l_z of the domain is set as 13.46 (about 5.93 times of the boundary-layer thickness δ at $x = 200$) to contain three pairs of the optimal inflow waves. Then the computational domain is decomposed into 120 Fourier modes in the spanwise direction. The norms of inflow perturbations ($\|\boldsymbol{u}'_{in}\|$) are scaled to 0.1 and 0.12, which correspond to maximum inflow perturbation velocities 6.4×10^{-2} and 7.6×10^{-2}, respectively. We have also confirmed that the streaky response of boundary layer is similar to the result of linear calculation when the norm of inflow perturbation is small ($\|\boldsymbol{u}'_{in}\| = 0.001$, not shown here).

Figure 15 shows the nonlinear response of the boundary-layer with $\|\boldsymbol{u}'_{in}\| = 0.12$. The streamwise vorticity strongly interacts with the streamwise streaks and the low-speed streaks are apparently lifted away from the surface whereas the high-speed streaks are shifted towards the surface owing to a nonlinear lift-up mechanism (Mao *et al.* 2017). The low-speed streaks have reached the edge of the boundary layer and are thus exposed to free-stream disturbances out of the boundary layer, as shown in figure 15(*a*). In the present case, the inflow perturbation is fixed at frequency $\omega = 2\pi/60$ and in the absence of high-frequency free-stream disturbances, the streaks do not undergo secondary instabilities such as meandering motions. However, the low-speed streaks on the vibrating plate are distorted in the vertical direction, which was not observed on fixed flat plate flow (Wang *et al.* 2019), whereas the high-speed streaks show a smooth profile. The distortion of low-speed streaks is attributed to the vibration of the plate and the unsteady nature of the perturbation. As has been shown in figure 12, the incoming unsteady streamwise vorticity ξ'_x is staggered by the vibrating plate to form the continuous ξ'_x and this continuity reduces in the vertical direction. In other words, the underlying sign-invariant ξ'_x is composed of continuous vorticity inside the boundary layer and become more unsteady or streamwise dependent around the edge of the boundary layer. As the low-speed streaks are lifted away from the wall by the nonlinear lift-up effect, they are exposed to the inhomogeneous streamwise vorticity around the edge of the boundary layer. The inhomogeneous vorticity at the top the boundary layer further stretches the low-speed streaks in the wall-normal direction. As a result, the low-speed streaks are streamwisely distorted. On the other hand, the high-speed streaks are shifted towards the wall by the nonlinear lift-up effect, so they are less affected by the streamwisely inhomogeneous vorticity at the top of the boundary layer and, thus, are not deformed.

The streamwise location of the distortion changes periodically with time owing to the convection effect. This can be also observed in figure 15(*b*), where the profiles of streaks over one vibrating period at $x = 150$ are illustrated. At $t = 270$, the nonlinear lift-up mechanism already manifested itself that the low-speed streaks are lifted above the high-speed streaks and show the mushroom shape. Then at $t = 285$, owing to the inhomogeneous streamwise vorticity (locally strong at some positions) at the top of the boundary layer, the low-speed streaks are distorted significantly whereas the high-speed streaks deform slightly. At $t = 300$ and $t = 315$, the low-speed streaks are further stretched in the wall-normal direction by the inhomogeneous streamwise vorticity, resulting in a slender cross-section of the low-speed streaks. At $t = 330$, the locally strong vorticity is convected downstream and the streaks have redeveloped to the mushroom shape again.

The streamwise development of the magnitude of the streaks is further studied to quantify this inhomogeneity induced distortion. According to the previous studies (Andersson *et al.* 2001; Brandt *et al.* 2004), the streak amplitude can be defined as

$$Am(x,t) = \frac{1}{2}\left[\max_{y,z}(u(x,y,z,t) - U(x,y,t)) - \min_{y,z}(u(x,y,z,t) - U(x,y,t))\right], \quad (5.1)$$

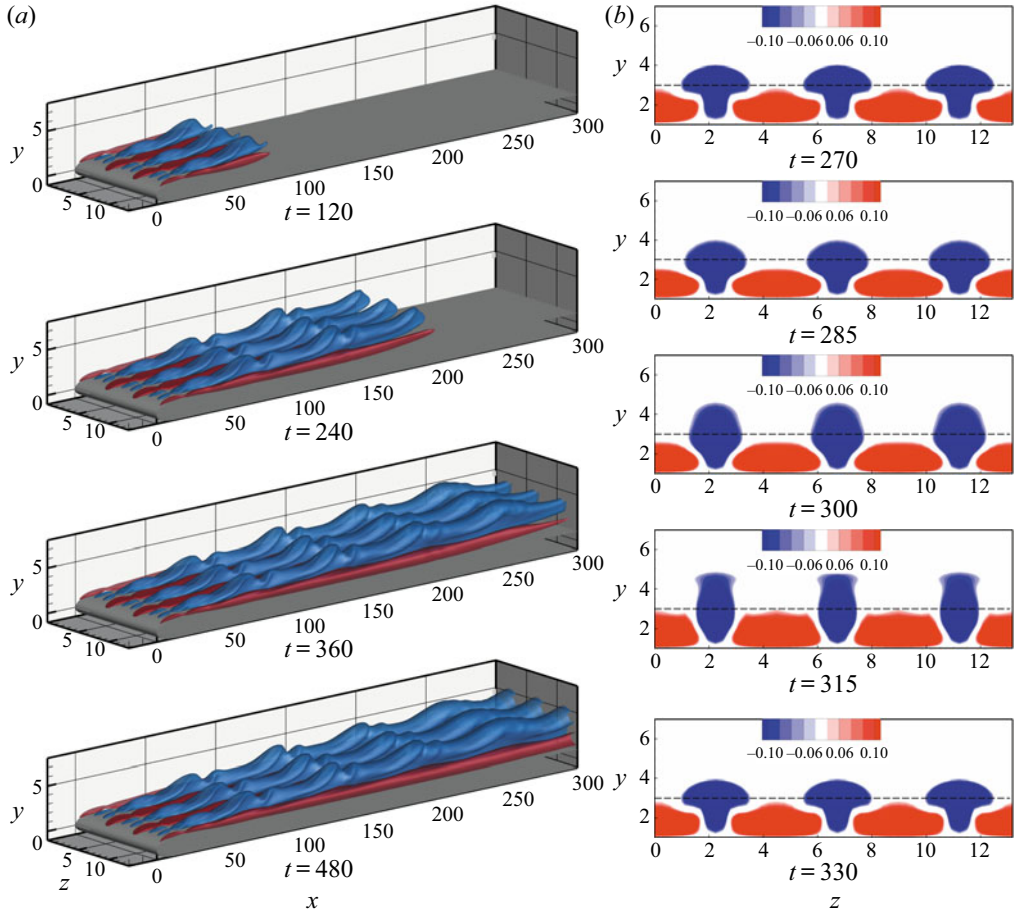

FIGURE 15. Nonlinear evolution of the inflow perturbations with time t. (a) 3-D view of isosurfaces of streamwise perturbation velocity $u' = 0.1$ and $u' = -0.1$ at $(Re, \omega, \omega_w, \|\boldsymbol{u}'_{in}\|) = (800, 2\pi/60, 2\pi/60, 0.12)$. The isosurfaces are colored by blue and red for $u' = -0.1$ and $u' = 0.1$, respectively. (b) Contours for u' extracted at $x = 150$. The dashed line in (b) marks the boundary-layer thickness, δ.

where $u(x, y, z, t)$ is the total streamwise velocity in the presence of streaks and $U(x, y, t)$ is the streamwise velocity of the base flow. It is also a function of time t because of the vibration. Variations of streak amplitude along x direction and the contours of ξ'_x at $t = 480$ are shown in figure 16. The continuous tilting of the base flow by ξ'_x gives rise to a trend of amplification of streaks in streamwise direction with strong fluctuations. When the inflow perturbations is strong with $\|\boldsymbol{u}'_{in}\| = 0.12$ and the plate is vibrating, the global maximum of streaks is located at $x = 125$ and its amplitude is 42.5 %. Further downstream, the streaks decay under the viscous effect. The fluctuation of streaks on the vibrating plate can, thus, be classified into three zones: growing ($x < 64$), mature ($64 < x < 127$) and decay ($x > 127$). In the growing zone, A_m grows quickly and the streamwise wavelength of streak fluctuation is approximately half of the wavelength of the inflow perturbation ($0.5 \times 2\pi U_\infty/\omega = 30$). The explanation of this wavelength is given later. In the mature zone, the magnitude of the streaks reaches maximum with the oscillation frequency reducing. In the decay zone, the viscosity dissipation results in a

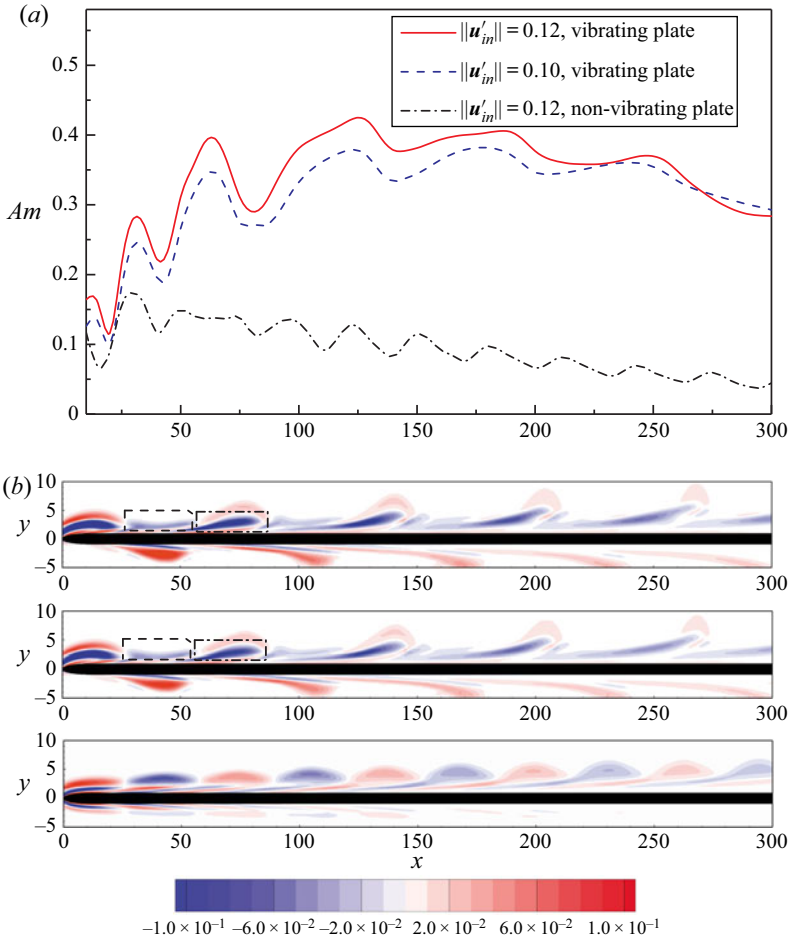

FIGURE 16. (*a*) Variation of streak amplitude Am with x and (*b*) contours of ξ'_x at $t = 480$. The dash-dotted box marks ξ'_{x1} and the dashed box marks ξ'_{x2}. The optimal inflow perturbations are obtained at $(Re, \omega, \omega_w) = (800, 2\pi/60, 2\pi/60)$. The contours from top to down correspond to cases at $\|\boldsymbol{u}'_{in}\| = 0.12$, on vibrating plate, $\|\boldsymbol{u}'_{in}\| = 0.1$, on vibrating plate, and $\|\boldsymbol{u}'_{in}\| = 0.12$, on non-vibrating plate.

downward trend of the streak amplitude and the fluctuation of streak amplitude is also smaller. Similar evolution of A_m is found when the norm of the inflow perturbation is scaled to 0.1. The difference is that the streaks decay slower and the global maximum of A_m is obtained at larger x around 170. To summarize, even if the streaks show an invariant sign owing to the synchronized motion revealed in § 4.3, their magnitude is periodically modulated by the vibration of the plate. For the non-vibrating case, the growing zone is smaller ($x < 30$) and the decay zone is longer ($x > 90$).

The inhomogeneous distribution of ξ'_x is shown in figure 16(*b*) to explain the fluctuation of A_m. In § 4.3, we have classified the streamwise vorticity on the upper side of the plate into two components, ξ'_{x1} and ξ'_{x2}, representing the streamwise vorticity entering the upper boundary layer when the plate is moving downward and upward, respectively. For clarity, in the first two rows of figure 16(*b*) (the nonlinear counterpart of figure 12*b*), ξ'_{x1} and ξ'_{x2} are marked by dash-dotted box and dashed box, respectively. The fluctuation of A_m shown

in figure 16(*a*) is in accordance with the inhomogeneity of ξ_x' shown in figure 16(*b*), which indicates the influence of inhomogeneous ξ_x' on the nonlinear lift-up mechanism. Take the vibrating case with $\|\boldsymbol{u}_{in}'\| = 0.12$ as an example, the streak amplitude A_m is plotted in figure 16(*a*) as the red solid line and the streamwise vorticity is shown in the top row of figure 16(*b*). These two figures show that the local peak of streak amplitude at $x \approx 125$ is in accordance with the locally strong ξ_x' at $x \approx 125$. Similar features can also be seen at $x \approx 185$ and $x \approx 245$. Later, we discuss the fluctuation of the streak amplitude in different zones in details. In the growing zone, both ξ_{x1}' and ξ_{x2}' are strong and capable of amplifying the streak. Therefore, for the vibrating plate, the fluctuation of A_m in this zone is due to the alternation of ξ_{x1}' and ξ_{x2}'. Thus, the streamwise wavelength of A_m is half of the streamwise wavelength of the inflow perturbation. For the non-vibrating plate, the fluctuation is attributed to the alternation of positive and negative streamwise vorticity (unsteadiness of the inflow perturbation). In the mature zone, ξ_{x2}' on the vibrating plate is decaying and, thus, the alternation of ξ_{x1}' and ξ_{x2}' does not lead to any sharp increase of A_m for the vibrating case. For the stationary case, the pattern of the streamwise vorticity is unchanged but the streak amplitude has reached the global peak value and starts to decrease. In the decay zone, the weaker streamwise vorticity under the viscous effect results in smaller fluctuation of A_m. For the vibrating plate, the wavelength of fluctuation in decay zone is close to the wavelength of inflow perturbations ($2\pi U_\infty/\omega = 60$) because only ξ_{x1}' can lead to a sudden increase of A_m in this zone, whereas ξ_{x2}' is weak and confined inside the boundary layer. For the non-vibrating plate, the wavelength of fluctuation in the decay zone remains unchanged because the pattern of ξ_x' is the same as that in the growing zone and mature zone (see figure 16(*b*), the last row) and the streak amplitude reduces to less than 0.05 at $x = 300$.

The periodical distortion of streaks might lead to intermittent secondary instabilities. As discussed in the previous section, the lifted low-speed streaks are prone to secondary instabilities seeded by high-frequency disturbances in the free stream. In order to activate the secondary instability of streaks and transition to turbulence, high-frequency disturbances are added to the optimal inflow perturbations to perturb the flow. The high-frequency disturbances consist of Fourier waves with the form

$$u_h' = \sum_{j=2}^{J}\sum_{m=0}^{M}\sum_{n=0}^{N}\eta_{jmn}\sin(\gamma_n \cdot y)\cos(\beta \cdot m \cdot z)\mathrm{e}^{\mathrm{i}j\omega t}, \tag{5.2}$$

where $m \cdot \beta$ is the spanwise wavenumber of the mth spanwise wave and γ_n is the arbitrary wall-normal wavenumber of the nth wall-normal wave. The high-frequency disturbances consist of 48 spanwise waves and 15 wall-normal waves ($M = 48,\ N = 15$). Here η_{jmn} is the random amplitude of the high-frequency noise satisfying $\sqrt{\sum \eta_{jmn}^2} = 0.015$, and $j\omega$ is the disturbance frequency. The frequency of the inflow perturbation that gives rise to the velocity streaks is $\omega = 2\pi/60$. Here the high-frequency disturbances are made up of 72 modes ($J = 72$). The nonlinear response of the boundary layer is traced by performing 3-D DNS and the results are shown in figure 17. For comparison, the response of the boundary-layer on stationary plate (figure 17*a*) as well as response to smaller-amplitude perturbations (figure 17*b*) are also plotted. The corresponding velocity perturbations are shown in figure 17(*d–f*).

The streaks on the stationary plate do not breakdown, and they are finally attenuated by viscous effects in the absence of secondary instabilities (see figure 17*d*). In the previous studies by Andersson *et al.* (2001) and Zaki & Durbin (2006), the instability of streaks

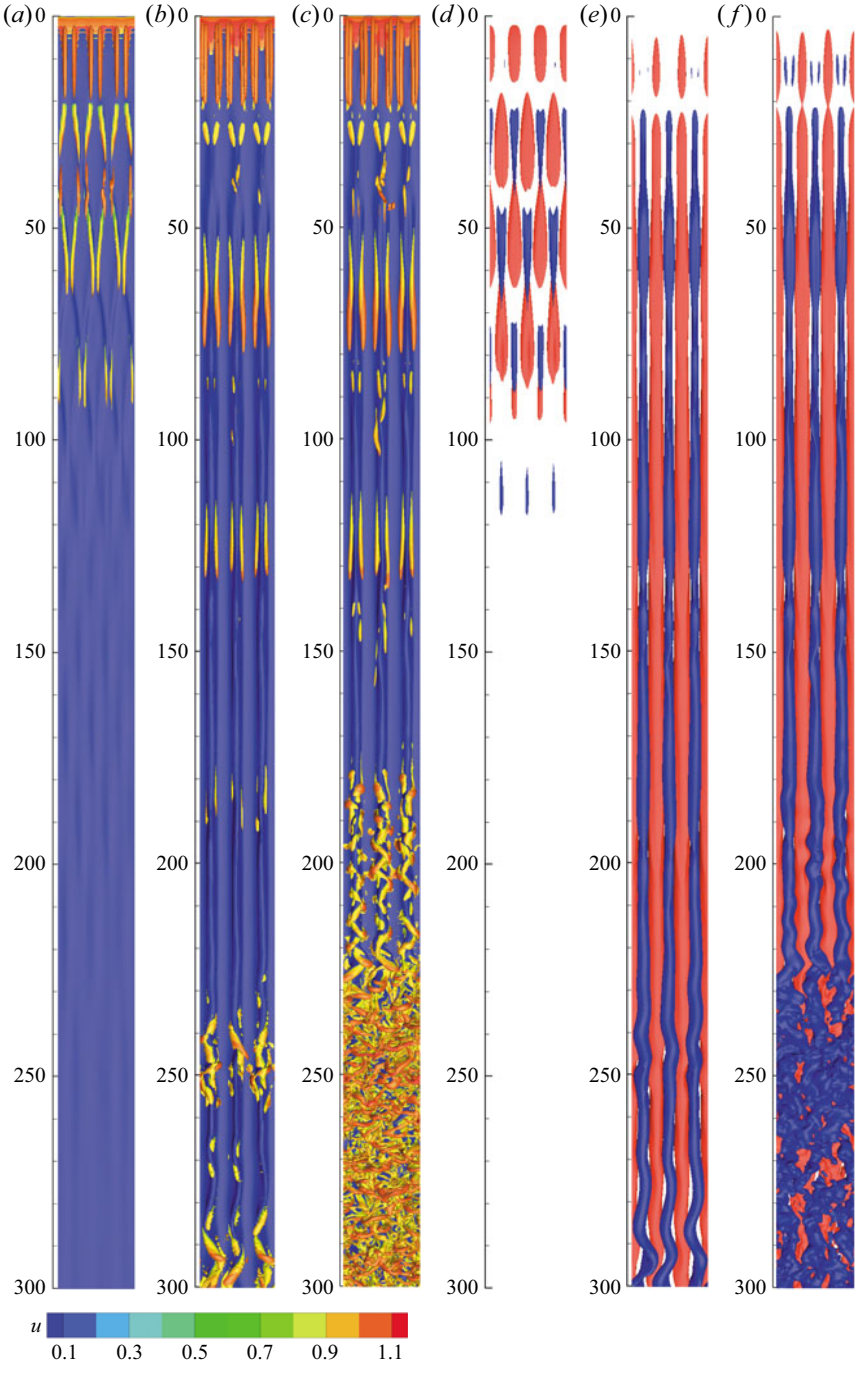

FIGURE 17. Top view of isosurfaces of instantaneous flow fields after adding higher-frequency inflow disturbance :(a, d) $(A, \omega, \omega_w, \|\boldsymbol{u}'_{in}\|) = (0, 2\pi/60, 2\pi/60, 0.12)$, ($b$, e) $(A, \omega, \omega_w, (\|\boldsymbol{u}'_{in}\|) = (0.01, 2\pi/60, 2\pi/60, 0.1)$ and (c,f) $(A, \omega, \omega_w, \|\boldsymbol{u}'_{in}\|) =(0.01, 2\pi/60, 2\pi/60, 0.12)$. ($a$)–($c$) Isosurfaces of $\lambda_2 = \{-0.01, 0.005, 0.002\}$ colored by the full velocity, using the isosurfaces of streamwise velocity $u = 0.8$ as the background. (d)–(f) Isosurfaces of streamwise perturbation $u' = \pm 0.12$.

is related to the inflectional point of the velocity profile. For the sinuous mode, the instability of streaky boundary layer is related to the spanwise shear induced by the streaks, whereas for the varicose mode, the instability is in connection with the wall-normal shear (Saric 1994; Asai *et al.* 2002). The low- and high-speed streaks alternately appear in the streamwise direction and overlap with each other inside the boundary layer (the heads of the low-speed streaks lay above the tails of the high-speed streaks and vice versa) when the plate is stationary, causing strong wall-normal shear. Therefore, the streaks on the stationary plate are prone to the varicose-type instability. Vaughan & Zaki (2011) argued that the inner mode (varicose type) was stable in low-amplitude, higher-frequency streaks. In our study, the normalized frequency ($F = 10^6\omega/\sqrt{U_\infty x/\nu}$) of streaks at $x = 300$ is $F = 214$, which is outside of the most energetic frequency range ($0 < F < 100$) (Jacobs & Durbin 2001; Vaughan & Zaki 2011) and the amplitude of the streak is small ($A_m = 0.05$). Therefore, the inner mode instability of the streaks on the stationary plate is still too weak to arouse the streaks to breakdown and form the turbulent spots. In another study with the same geometry and Reynolds number as those in the present work, bypass transition was achieved by combining the inflow perturbations and a body forcing (Wang *et al.* 2019).

The secondary instabilities of streaks are successfully stimulated by the high-frequency disturbances for the vibrating plate flow (see figure 17*b*,*e*). The meandering motions of streaks are spotted at $x \approx 95$, 150, 200, 250 and 300 and the meandering becomes more intense as x increases, indicating that the secondary instability of streaks is intermittent and growing in every period. The interruption of the secondary instabilities of streaks is attributed to the inhomogeneity of streamwise vorticity around the edge of the boundary layer, which breaks the mushroom shape of the low-speed streaks periodically. From the λ_2 (Jeong & Hussain 1995) plot at $x \approx 250$ and 300, the meandering motions of streaks are asymmetric, suggesting that the secondary instability is of the sinuous type (see figure 17*c*). The meandering does not appear at the position where a local peak of streak amplitude appears. Instead, it appears at the positions where the cross-section of the streak is of mushroom shape. The streak amplitudes at the positions where the meandering is observed ($x = 95$, 150, 200, 250, 300) are 0.31, 0.34, 0,35, 0.35, 0.29 at perturbation level $\|\boldsymbol{u}'_{in}\| = 0.1$. The streak amplitude around 300 is smaller, but the meandering motion of the streaks becomes stronger (see figure 17*e*). In fact, it has been found that the streaky boundary layer could be more unstable when the cross-section of low-speed streaks are altered into trapezoidal shape (wide at the top and narrow at the bottom), even though its amplitude is decreased slightly (Wang *et al.* 2019). The result presented previously agrees with this observation.

The streaks finally break down and the transition is triggered as the perturbation level is increased to $\|\boldsymbol{u}'_{in}\| = 0.12$. The meandering motions of the streaks occur at $x \approx 95$, 150 and 200 and the corresponding streak amplitudes are 0.36, 0.38 and 0.37. The secondary instability after $x = 200$ is strong enough to sustain itself even if the cross-section of the streaks is slightly stretched (see the meandering motions of the streaks at $x = 210$ and 220). While for the smaller perturbation level, the development of instability is interrupted when the cross-section of the mushroom shape of the streak is broken. For the streaky boundary layer over the stationary plate perturbed by steady perturbation, the meandering occurs at $x = 101$ where A_m is 0.35 (Wang *et al.* 2019). In comparison with their result, although the onset of secondary instability is observed at a similar streamwise location and streak amplitude (the meandering motions of the streaks are spotted at $x = 95$ where $A_m = 0.36$), the transition process over the vibrating plate is prolonged. The breakdown of streaks and the onset of transition are quick after the burst of secondary instability for stationary plate flow, while for the vibrating plate, the streaks undergo several rounds of instabilities before the onset of transition.

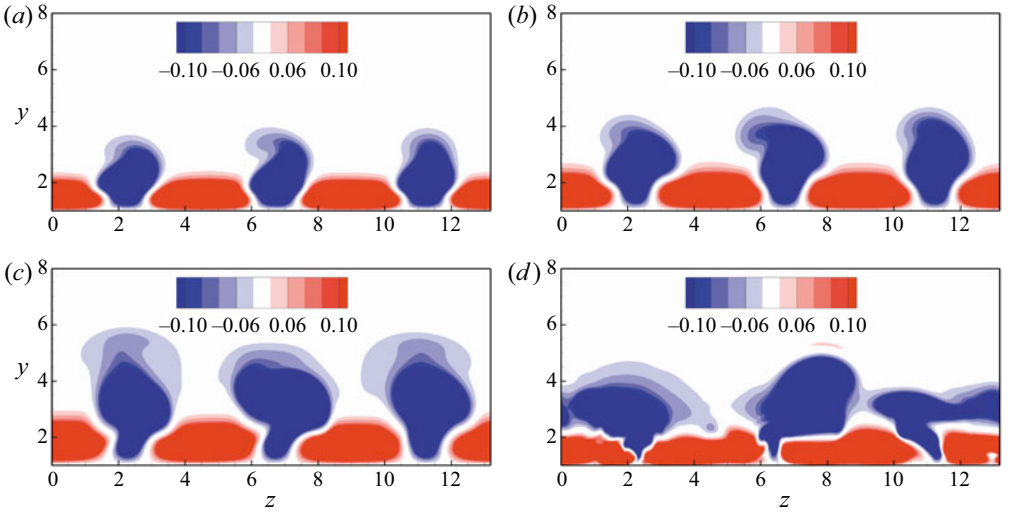

FIGURE 18. Contour for u' at various streamwise locations after adding higher-frequency noise, (*a*) $x = 95$, (*b*) $x = 150$, (*c*) $x = 200$ and (*d*) $x = 230$. The result is obtained at $(t, \omega, \omega_w, \|\boldsymbol{u}'_{in}\|) = (480, 2\pi/60, 2\pi/60, 0.12)$.

The cross-sections of the streaky boundary layer at $x = 95$, 150, 200 and 230 are shown in figure 18 to illustrate the details of the secondary instabilities. In general, it is clear that the cross-section of the streak is of mushroom shape when the secondary instabilities are stimulated. At $t = 95$, the low-speed streaks are lifted above the high-speed streaks and the periodicity in the spanwise direction is broken because of the secondary instabilities. The secondary instability at this position is weak and interrupted by the inhomogeneous nonlinear lift-up, so the spanwise periodicity of the low-speed streaks is recovered downstream. At $x = 150$, as the low-speed streaks are lifted higher owing to the lift-up, the influence of the inhomogeneous nonlinear lift-up becomes stronger and, thus, the low-speed streaks are further distorted. The distortion of the streaks is mainly in spanwise direction, manifesting the spanwise shear correlation of the sinuous-type instability. The secondary instability of streaks continues to develop at $x = 200$. The non-periodicity and the meandering motions of the streaks is so strong that the inhomogeneous nonlinear lift-up downstream cannot interrupt the spanwise distortion of the streaks. Further downstream at $x = 230$, the streaks break down as has been observed in figure 17.

The skin friction coefficients (C_f) for cases shown in figure 17 are plotted in figure 19. The black solid curve represent mean C_f for the periodic base flow, which is close to the theoretical laminar skin friction coefficient. Over half of the gap between the base flow C_f and the theoretical laminar C_f at larger streamwise location can be directly attributed to the pressure gradient downstream of the leading edge, because the present streamwise force should be $\tau_w - \partial p/\partial x$, where τ_w is the wall shear. For the non-vibrating plate ($A = 0$), the skin friction coefficient is increased slightly compared with the base case at $x \approx 50$ because of the presence of streamwise velocity streaks. Further downstream, the streaks decay and, thus, C_f remains at the laminar value for the rest of the plate. For the vibrating plate, the elongated streaks perturbed by weaker inflow disturbance ($\|\boldsymbol{u}'_{in}\| = 0.1$) also cause an increase of the skin friction coefficient. However, the streak amplitude is insufficient to trigger the inception of transition and, thus, the value of C_f falls down when the streaks are attenuated by viscosity. Once the base flow is perturbed by

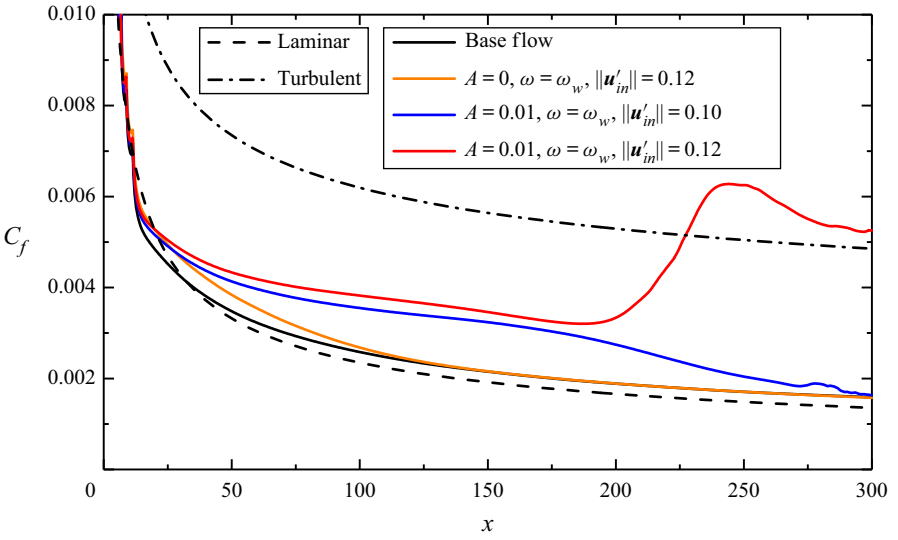

FIGURE 19. Skin friction coefficients (C_f) for various cases. Higher-frequency disturbances to the optimal inflow perturbation is added.

the strong resonant inflow perturbation ($\|\boldsymbol{u}'_{in}\| = 0.12$), the skin friction coefficient shoots up at $x \approx 230$, representing the onset of transition, before converging to the turbulent C_f curve. Compared with the stationary plate results (Nolan & Zaki 2013), the skin friction coefficient over the vibrating plate takes long distance to shoot up, indicating that the transition stage covers a larger area. Therefore, the vibration of the plate staggers the resonant inflow perturbation to produce the elongated streamwise streaks inside the boundary layer, which creates the precondition for the bypass transition. However, the inhomogeneous nonlinear lift-up caused by the vibration acts as a hindrance in the secondary instability excitation process.

6. Conclusions

The evolution of free-stream disturbance in flow over a vertically vibrating flat plate has been studied. The optimal amplification of the flow to inflow perturbations has been computed to investigate the effects of the plate vibration on the development of free-stream disturbance, secondary instability of streaks and subsequently the bypass transition to turbulence. Driven by the motion of the plate, the base flow is periodic in time and homogeneous in the spanwise direction.

In comparison with the non-vibrating case, the plate vibration reduces the global maximum gain of the inflow perturbation obtained at inflow frequency $\omega = 0$, suggesting that the linear lift-up process is suppressed by the vibration. For parameters considered here, the amplification of optimal inflow perturbations decreases monotonically as the vibration amplitude increases. As the vibration frequency is increased to $\omega_w = 2\pi/60$ and then $\omega_w = 2\pi/45$, the vibration induces an obvious second local peak on the contour plot of the gain K_{max} on the plane of spanwise wavenumber β and perturbation frequency ω, and this peak appears at $\omega = \omega_w$, suggesting resonance between the perturbation and the plate vibration. This resonance provides an opportunity for the high-frequency perturbations to enter the boundary layer. As a result, the cut-off frequency, above which the free-stream perturbation is shielded by the boundary layer, becomes higher.

The response of the boundary layer to the optimal perturbation shows that at the resonance condition with $\omega = \omega_w = 2\pi/60$, the perturbation structures over the vibrating plate are elongated streamwise streaks similar to the streaks induced by steady inflow perturbations over a stationary plate, whereas the unsteady inflow perturbation over the stationary plate are streamwise periodic streaks. By examining the perturbation velocity profile and the evolution history of the resonant inflow perturbations, it is found that the resonance phenomenon can be attributed to the continuous streamwise vorticity generated by the staggering effect of the vibrating plate. The optimal perturbation velocity profile at the resonant frequency consists of more layers in the vertical direction than that over the stationary plate. In other words, the streamwise velocity (vorticity) perturbation upstream of the leading edge consists of a positive and a negative component in the vertical direction. The upward/downward movement of the plate in one vibration cycle imposes a negative/positive angle of attack, which shifts the inflow perturbations toward the lower/upper side of the plate. For the resonant inflow perturbations, the downward movement of the plate shifts both the negative and positive components of inflow perturbations to the upper side of the plate and the negative (positive) part is in (out of) the upper boundary layer. While the upward movement of the plate shifts the negative component on the upper array of inflow disturbance to the upper side of the plate and displaces the positive component on the lower array to the lower side. This synchronization of the motion of the plate and the perturbation ensures that the streamwise vorticity in the upper boundary layer is sign invariant in the streamwise direction and, thus, capable of amplifying the streaks continuously. For steady inflow perturbations, the plate vibration tends to break the streamwise velocity into segments and thus weakens the lift-up mechanism. A similar staggering mechanism of a moving streamlined body can also be found in the study of flapping wings in the tandem configuration (Lua *et al.* 2016). The flapping of the wings also introduces a periodically varying angle of attack, which shifts the wake of the front wing to upside or downside of the rear wing.

The vertical vibration of the plate also affects the nonlinear lift-up and the secondary instability of the streaks. In the absence of high-frequency free-stream disturbances, the streaks do not present secondary instability such as meandering motions, but the low-speed streaks on the vibrating plate are apparently distorted in the vertical direction, which was not observed on stationary plate flow and can be attributed to the vibration of the plate. The sign-invariant streamwise vorticity in the upper boundary layer is composed of ξ'_{x1} and ξ'_{x2}, representing streamwise vorticity entering the upper boundary layer when the plate is moving downward and upward, respectively. Here ξ'_{x1} and ξ'_{x2} are continuous inside the boundary layer but become streamwisely periodic near the edge of the boundary layer, leading to the inhomogeneity of the strength of nonlinear lift-up around the edge of the boundary layer. As a consequence, the low-speed streaks are stretched in the wall-normal direction, and their distributions in the y–z plane become slender, deviating from the mushroom shape which is prone to lose stability. This distortion is periodic in time owing to the convection of the inhomogeneous nonlinear lift-up. After the inhomogeneity is convected downstream, the low-speed streaks redevelop into mushroom shape again. In other words, although the resonant inflow perturbation induces sign-invariant streaks over the vibrating plate owing to the synchronized motion of the plate and the perturbation, the magnitude and shape of the streaks are periodically modulated by the vibration of the plate.

The secondary instabilities of the streaks are intermittent because the periodic distortion of the streaks and the instabilities are of sinuous type as the meandering motions of the streaks are asymmetric. These instabilities are stimulated by adding high-frequency free-stream disturbances to the optimal inflow perturbation. The meandering motions

of streaks are spotted at $x = 95$, 150 and 200 with the magnitude gradually increasing, confirming that the secondary instabilities of streaks are intermittent and grow in every period. The meandering does not occur at the position where a local peak of the streak magnitude appears. Instead, it occurs at the position where the cross-section of the streak is of mushroom shape. It indicates that the intermittence of the secondary instability can be attributed to the inhomogeneity of the streamwise vorticity around the edge of boundary layer, which breaks the mushroom shape of the streaks and thus interrupts the secondary instability. As the perturbation level is increased to $\|\boldsymbol{u}'_{in}\| = 0.12$, the instability of streaks after $x = 200$ is strong enough to sustain itself even if the shape of streaks is slightly stretched, and the onset of transition finally occurs. Compared with the streak instability and breakdown over a stationary plate, the burst of secondary instabilities over a vibrating plate is observed at a similar streamwise location and streak amplitude, but the streaks undergo several rounds of instability before the onset of transition. As a consequence, the nonlinear deformation of streaks or the transition stage occupies a larger streamwise distance as indicated by the C_f curve, illustrating the importance of considering the vibration effect when modelling or predicting the bypass transition in boundary-layer flow over a vibrating body.

Acknowledgements

We would like to acknowledge the financial support from the Key Research and Development Program of Shaanxi in China (program number 2018KW-017), and from the European Union's Horizon 2020 research and innovation programme under Marie Skłodowska-Curie grant agreement number 777717. Part of the calculations were performed on HPC-Midlands funded by the Engineering and Physical Sciences Research Council (grant number EP/K000063/1).

Declaration of interests

The authors report no conflict of interest.

Supplementary movies

Supplementary movies are available at https://doi.org/10.1017/jfm.2020.923.

REFERENCES

ALFREDSSON, P. H. & MATSUBARA, M. 1996 Streaky structure in transition. In *Transitional Boundary Layers in Aeronautics* (ed. M. Henkes & J. L. van Ingen), pp. 374–386. Elsevier.

ANDERSSON, P., BERGGREN, M. & HENNINGSON, D. S. 1999 Optimal disturbances and bypass transition in boundary layers. *Phys. Fluids* **11**, 134–150.

ANDERSSON, P., BRANDT, L., BOTTARO, A. & HENNINGSON, D. S. 2001 On the breakdown of boundary layer streaks. *J. Fluid Mech.* **428**, 29–60.

ASAI, M., MINAGAWA, M. & NISHIOKA, M. 2002 The instability and breakdown of low-speed streak. *J. Fluid Mech.* **455**, 289–314.

BALAMURUGAN, G. & MANDAL, A. C. 2017 Experiments on localized secondary instability in bypass boundary layer transition. *J. Fluid Mech.* **817**, 217–263.

BARON, A. & QUADRIO, M. 1996 Turbulent drag reduction by spanwise wall oscillation. *Appl. Sci. Res.* **55**, 311–326.

BLACKBURN, H. M. & SHERWIN, S. J. 2004 Formulation of a Galerkin spectral element–Fourier method for three-dimensional incompressible flows in cylindrical geometries. *J. Comput. Phys.* **197** (2), 759–778.

BRANDT, L., SCHLATTER, P. & HENNINGSON, D. S. 2004 Transition in boundary layers subject to free-stream turbulence. *J. Fluid Mech.* **517**, 167–198.

BRANDT, L., SIPP, D., PRALITS, J. O. & MARQUET, O. 2011 Effect of base-flow variation in noise amplifiers: the flat-plate boundary layer. *J. Fluid Mech.* **687**, 503–528.

BUTLER, K. M. & FARRELL, B. F. 1992 Three-dimensional optimal perturbations in viscous shear flow. *Phys. Fluids* **4**, 1637–1650.

CHOI, K. S. 2002 Near wall structure of turbulent boundary layer with spanwise-wall oscillation. *Phys. Fluids* **14** (7), 2530–2542.

CHOI, H., MOIN, P. & KIM, J. 1994 Active turbulence control for drag reduction in wall bounded flows. *J. Fluid Mech.* **262**, 75–110.

FRANSSON, J. H. M. & ALFREDSSON, P. H. 2003 On the disturbance growth in an asymptotic suction boundary layer. *J. Fluid Mech.* **482**, 51–90.

FUCIARELLI, D., REED, H. & LYTTLE, I. 2000 Direct numerical simulation of leading-edge receptivity to sound. *AIAA J.* **38** (7), 1159–1165.

HACK, M. J. P. & ZAKI, T. A. 2012 The continuous spectrum of time-harmonic shear layers. *Phys. Fluids* **24**, 034101.

HACK, M. J. P. & ZAKI, T. A. 2014 The influence of harmonic wall motion on transitional boundary layer. *J. Fluid Mech.* **760**, 63–94.

HACK, M. J. P. & ZAKI, T. A. 2015 Modal and non-modal stability of boundary layers forced by spanwise wall oscillations. *J. Fluid Mech.* **778**, 389–427.

HAMMERTON, P. W. & KERSCHEN, E. J. 1996 Boundary-layer receptivity for a parabolic leading edge. *J. Fluid Mech.* **310**, 243–267.

HUNT, J. C. R. & DURBIN, P. A. 1999 Perturbed vortical layers and shear sheltering. *Fluid Dyn. Res.* **24**, 375–404.

JACOBS, R. G. & DURBIN, P. A. 2001 Simulations of bypass transition. *J. Fluid Mech.* **428**, 185–212.

JEONG, J. & HUSSAIN, F. 1995 On the identification of a vortex. *J. Fluid Mech.* **285**, 69–94.

JUNG, W. J., MANGIVACCHI, N. & AKHAVAN, R. 1992 Suppression of turbulence in wall-bounded flows by high-frequency spanwise oscillations. *Phys. Fluids* A **4** (8), 1605–1607.

KAMETANI, Y. & FUKAGATA, K. 2011 Direct numerical simulation of spatially developing turbulent boundary layers with uniform blowing or suction. *J. Fluid Mech.* **681**, 154–172.

KARNIADAKIS, G. E. & CHOI, K. S. 2003 Mechanisms in transverse motions in turbulent wall flows. *Annu. Rev. Fluid Mech.* **35**, 45–62.

KARNIADAKIS, G. & SHERWIN, S. J. 2007 *Spectral/HP Element Methods for Computational Fluid Dynamics*. Oxford University Press.

KENDALL, J. M. 1985 Experiment study of disturbances produced in a pre-transitional laminar boundary layer by weak freestream turbulence. *AIAA Paper* 85-1695. American Institute of Aeronautics and Astronautics.

LAADHARI, F., SKANDAJI, L. & MOREL, R. 1994 Turbulence reduction in a boundary layer by a local spanwise oscillating surface. *Phys. Fluids* **6** (10), 3218–3220.

LANDAHL, M. T. 1975 Wave breakdown and turbulence. *SIAM J. Appl. Maths* **28** (4), 735–756.

LANDAHL, M. T. 1980 A note on an algebraic instability of inviscid parallel shear flows. *J. Fluid Mech.* **98**, 1–34.

LUA, K. B., LU, H., ZHANG, X. H., LIM, T. T. & YEO, K. S. 2016 Aerodynamics of two-dimensional flapping wings in tandem configuration. *Phys. Fluids* **28**, 121901.

LUCHINI, P. 2000 Reynolds-number-independent instability of the boundary layer over a flat surface: optimal perturbations. *J. Fluid Mech.* **404**, 289–309.

MANDAL, A. C., VENKATAKRISHNAN, L. & DEY, J. 2010 A study on boundary-layer transition induced by free-stream turbulence. *J. Fluid Mech.* **660**, 114–146.

MANS, J., KADIJK, E. C., LANGE, H. C. & VAN STEENHOVEN, A. A. 2005 Breakdown in a boundary layer exposed to free-stream turbulence. *Exp. Fluids* **39**, 1071.

MAO, X., BLACKBURN, H. M. & SHERWIN, S. J. 2013 Calculation of global optimal initial and boundary perturbations for the linearised incompressible Navier–Stokes equations. *J. Comput. Phys.* **235**, 258–273.

MAO, X., SHERWIN, S. J. & BLACKBURN, H. M. 2011 Transient growth and bypass transition in stenotic flow with a physiological waveform. *Theor. Comput. Fluid Dyn.* **25**, 31–42.

MAO, X., ZAKI, T. A., BLACKBURN, H. M. & SHERWIN, S. J. 2017 Transition induced by linear and nonlinear perturbation growth in flow past a compressor blade. *J. Fluid Mech.* **820**, 604–632.

MATSUBARA, M. & ALFREDSSON, P. 2001 Disturbance growth in boundary layers subjected to free-stream turbulence. *J. Fluid Mech.* **430**, 149–168.

MONOKROUSOS, A., ÅKERVIK, E., BRANDT, L. & HENNINGSON, D. S. 2010 Global three-dimensional optimal disturbances in the Blasius boundary-layer flow using time-steppers. *J. Fluid Mech.* **650**, 181–214.

MORKOVIN, M. V. 1969 On the many faces of transition. In *Viscous Drag Reduction* (ed. C. S. Wells), pp. 1–31. Springer.

NAGARAJAN, S., LELE, S. K. & FERZIGER, J. H. 2007 Leading-edge effects in bypass transition. *J. Fluid Mech.* **572**, 471–504.

NOLAN, K. P. & WALSH, E. J. 2012 Particle image velocimetry measurements of a transitional boundary layer under free stream turbulence. *J. Fluid Mech.* **702**, 215–238.

NOLAN, K. P. & ZAKI, T. A. 2013 Conditional sampling of transitional boundary layer in pressure gradients. *J. Fluid Mech.* **728**, 306–339.

OLINGER, D. J. & SREENIVASAN, K. R. 1988 Nonlinear dynamic of the wake of an oscillating cylinder. *Phys. Rev. Lett.* **60**, 797–800.

PAMIÈS, M., GARNIER, E., MERLEN, A. & SAGAUT, P. 2007 Response of a spatially developing turbulent boundary layer to active control strategies in the framework of opposition control. *Phys. Fluids* **19**, 108102.

REDDY, S. C. & HENNINGSON, D. S. 1993 Energy growth in viscous channel flows. *J. Fluid Mech.* **252**, 209–238.

RICCO, P. 2011 Laminar streaks with spanwise wall forcing. *Phys. Fluids* **22**, 064103.

RILEY, N. 1965 Oscillating viscous flow. *Mathematika* **12**, 161–175.

RILEY, N. 1967 Oscillating viscous flow. review and extension. *IMA J. Appl. Maths* **3** (4), 419–434.

SARIC, W. S. 1994 Görtler vortices. *Annu. Rev. Fluid Mech.* **26**, 379–409.

SCHRADER, L. U., BRANDT, L., MAVRIPLIS, C. & HENNINGSON, D. S. 2010 Receptivity of free-stream vorticity of flow past a flat plate with elliptic leading edge. *J. Fluid Mech.* **653**, 245–271.

SPALART, P. R. 1989 Theoretical and numerical study of a three dimensional turbulent boundary layer. *J. Fluid Mech.* **205**, 319–340.

SWEARINGEN, J. D. & BLACKWELDER, R. F. 1987 The growth and breakdown of streamwise vortices in the presence of a wall. *J. Fluid Mech.* **182**, 255–290.

TOUBER, E. & LESCHZINER, M. A. 2012 Near-wall streak modification by spanwise oscillatory wall motion and drag-reduction mechanisms. *J. Fluid Mech.* **507**, 1–51.

VAUGHAN, N. J. & ZAKI, T. A. 2011 Stability of zero-pressure-gradient boundary layer distorted by unsteady Klebanoff streaks. *J. Fluid Mech.* **681**, 116–153.

WANDERLEY, J. B. V. & CORKE, T. C. 2001 Boundary layer receptivity to free-stream sound on elliptic leading edges of flat plates. *J. Fluid Mech.* **429**, 1–21.

WANG, B., MAO, X. & ZAKI, T. A. 2019 Low-frequency selectivity in flat-plate boundary layer with elliptic leading edge. *J. Fluid Mech.* **866**, 239–262.

WESTIN, K. J. A., BOIKO, A. V., KLINGMANN, B. G. B., KOZLOV, V. V. & ALFREDSSON, P. H. 1994 Experiments in a boundary layer subjected to free stream turbulence. Part 1. Boundary layer structure and receptivity. *J. Fluid Mech.* **281**, 193–218.

XIAO, D. & PAPADAKIS, G. 2019 Nonlinear optimal control of transition due to a pair of vortical perturbations using a receding horizon approach. *J. Fluid Mech.* **861**, 524–555.

ZAKI, T. A. & DURBIN, P. A. 2005 Mode interaction and the bypass route to transition. *J. Fluid Mech.* **531**, 85–111.

ZAKI, T. A. & DURBIN, P. A. 2006 Continuous mode transition and the effects of pressure gradients. *J. Fluid Mech.* **563**, 357–388.

ZAKI, T. A. & SAHA, S. 2009 On shear sheltering and the structure of vortical modes in single and two-fluid boundary layers. *J. Fluid Mech.* **626**, 111–147.